UNIVERSIDAD DE CHILE
FACULTAD DE CIENCIAS FÍSICAS Y MATEMÁTICAS
DEPARTAMENTO DE GEOLOGÍA

STABLE ISOTOPE AND ANTHROPOGENIC TRACER SIGNATURE OF WATERS IN AN ANDEAN GEOTHERMAL SYSTEM

TESIS PARA OPTAR AL GRADO DE MAGÍSTER EN CIENCIAS, MENCIÓN GEOLOGÍA
MEMORIA PARA OPTAR AL TÍTULO DE GEÓLOGO

RODRIGO FRANCISCO PÉREZ MORENO

PROFESOR GUÍA:
MARTIN REICH MORALES

MIEMBROS DE LA COMISIÓN:
LINDA DANIELE
DIEGO MORATA CÉSPEDES

Este trabajo ha sido financiado por el Centro de Excelencia en Geotermia de los Andes (CEGA), proyecto FONDAP-CONICYT 15090013, y por el Núcleo Milenio Trazadores de Metales NC130065

SANTIAGO DE CHILE
2019

SUMMARY OF THE THESIS FOR THE DEGREE OF:
MASTER OF SCIENCE IN GEOLOGY
BY: RODRIGO FRANCISCO PÉREZ MORENO
DATE: 2019
ADVISOR: MARTIN REICH MORALES

STABLE ISOTOPE AND ANTHROPOGENIC TRACER SIGNATURE OF WATERS IN AN ANDEAN GEOTHERMAL SYSTEM

In the present study, we combined stable isotopes and anthropogenic tracers to investigate the origin, residence times, and evolution of thermal waters in the Lonquimay-Tolhuaca Volcanic Complex (LTVC) of the southern Chilean Andes. A total of 20 groundwater samples from springs discharging at a broad range of temperatures (8–96 °C) were collected and analyzed for major ion geochemistry, stable isotope ratios (δ^2H, δ^{18}O, $\delta^{13}C_{TDIC}$), dissolved chlorofluorocarbons (CFCs) and sulfur hexafluoride (SF_6).

In addition, we compiled all available data on the isotopic composition of precipitation in the region to derive the local meteoric water line. Coupled with a Rayleigh-fractionation model of precipitation, we provide constraints on the elevation at which infiltration and recharge to the system is produced. $\delta^{13}C_{TDIC}$ values are consistent with the bulk of dissolved inorganic carbon being derived from the addition of soil CO_2 to an atmospheric source, while magma degassing and boiling processes are evidenced in samples discharging directly on the flanks of volcanoes. The isotopic composition of thermal water, once heated at depth, is further modified by CO_2 degassing and carbonate precipitation during ascent. All geothermal samples contain low but detectable concentrations of CFC-11, CFC-12, CFC-113, and SF_6, suggesting the addition of only a small fraction (2 to 22%) of modern meteoric water. The discharge temperature of naturally outflowing springs in the LTVC correlates directly with the age distribution of the water samples. This difference in residence times is attributed to the distinct subsurface circulation pathways of each water type—i.e., the shallow, diffuse flow of cold groundwater vs. the deep, focused circulation of thermal water along fault zones. Conduit flow along high vertical permeability networks allows hydrothermal fluid to remain relatively unmixed with shallow meteoric water during ascent.

Data from this study confirm that fault-fracture meshes with different orientations exert a first order control on the residence times, ascent, and mixing rates of thermal waters in this segment of the Andean Cordillera, thus modulating their chemical and isotopic signature. Additionally, our results show that the combined use of conventional hydrogeochemical and isotopic data with environmental tracers, including anthropogenic CFCs and SF_6, is a powerful tool to better understand the dynamics of geothermal systems.

RESUMEN DE LA TESIS PARA OPTAR AL TÍTULO DE:
MAGÍSTER EN CIENCIAS, MENCIÓN GEOLOGÍA
POR: RODRIGO FRANCISCO PÉREZ MORENO
FECHA: 2019
PROF. GUÍA: MARTIN REICH MORALES

ISÓTOPOS ESTABLES Y TRAZADORES ANTROPOGÉNICOS EN LAS AGUAS DE UN SISTEMA GEOTERMAL ANDINO

El presente trabajo se centra en el uso de isótopos estables y trazadores antropogénicos para investigar el origen, los tiempos de residencia y la evolución de las aguas termales en el Complejo Volcánico Lonquimay-Tolhuaca, ubicado en la parte central de la Zona Volcánica Sur. Veinte muestras de agua subterránea, surgiendo en un amplio rango de temperaturas (8–96 °C), son analizadas para determinar su composición química, incluyendo elementos mayores, razones isotópicas (δ^2H, δ^{18}O, $\delta^{13}C_{TDIC}$), y la concentración de clorofluorocarbonos (CFCs) y hexafluoruro de azufre (SF_6) disueltos.

Adicionalmente, se presenta un compilado de toda la información disponible sobre la composición isotópica de la precipitación en la región de la Araucanía. Mediante un modelo de fraccionamiento de Rayleigh aplicado a los isótopos de oxígeno, se logra constreñir la elevación a la cual se produce la recarga del sistema. Los valores de $\delta^{13}C_{TDIC}$ en las aguas indican la adición de CO_2 del suelo a una fuente de origen atmosférico en la mayoría de las muestras. No obstante, procesos de ebullición y desgasificación magmática se evidencian en las surgencias termales ubicadas en los flancos de volcanes. La composición isotópica de las aguas termales, una vez calentadas en profundidad, es modificada posteriormente por procesos de desgasificación de CO_2 y precipitación de carbonatos durante su ascenso. Todas las muestras de aguas termales presentan concentraciones bajas pero detectables de CFC-11, CFC-12, CFC-113 y SF_6, lo que sugiere la adición de una pequeña fracción (2 a 22 %) de agua meteórica moderna al sistema. La temperatura de surgencia de las aguas termales en el Complejo Volcánico Lonquimay-Tolhuaca se relaciona directamente con la distribución de edad en las muestras. Estas diferencias en los tiempos de residencia se atribuyen a los distintos mecanismos de circulación de cada tipo de agua: por un lado, las aguas frías poseen tiempos de residencia cortos y evidencian una circulación somera a través de un medio poroso, mientras que las aguas termales poseen tiempos de residencia mayores y evidencian un flujo canalizado a través de zonas de falla. El flujo de las aguas termales a través de estos conductos de alta permeabilidad vertical impide que sean diluidas con agua meteórica durante el ascenso.

Los datos de este estudio confirman que las redes de fallas y fracturas con distintas orientaciones ejercen un control sobre los tiempos de residencia, el ascenso y las tasas de mezcla de distintos fluidos en este segmento de la Cordillera de los Andes, determinando así su composición química e isotópica. Asimismo, nuestros resultados muestran que el análisis geoquímico e isotópico convencional, en conjunto con el uso de trazadores ambientales (incluyendo los trazadores antropogénicos, CFC y SF_6) son una poderosa herramienta para entender la dinámica hídrica de los sistemas geotermales.

For my parents

Acknowledgments

Foremost, I wish to thank the members of my dissertation committee: Martin Reich, Linda Daniele, and Diego Morata for their excellent support, guidance, and good will throughout these years. I consider myself fortunate to have worked under such extraordinary researchers and caring individuals, who helped nurture my love for science. I would especially like to thank my advisor, Martin, for his outstanding commitment as a professor, for being a true mentor, and for his trust in me by allowing me to lead this research project.

I would like to extend very sincere and heartfelt thanks to my co-authors: Sebastian Held and Jackie Wrage, who not only provided thoughtful comments and discussions during the preparation of this document, but whose work has always been an inspiration and constitutes the cornerstone of my research.

I wish to express great appreciation to: Verónica Rodríguez, Erika Rojas, and Samuel Lepe of the CEGA laboratory, for their kind support with the geochemical analyses, and Dr. Harald Oster of the *Spurenstofflabor*, for his swift and efficient work in tracer analysis. To Alberto Espinoza, of Transmark Renewables, for a shared passion on geothermal energy and many fruitful discussions regarding the Tolhuaca geothermal system. My most sincere thanks go to David Parkhurst, for co-creating the excellent PHREEQC program, and continuously offering technical and scientific support at phreeqcusers.org. Though there are too many to name, much appreciation goes to many landowners who generously provided access to springs for sample collection.

This thesis would not have been possible without the financial support from FONDAP project 15090013 "Centro de Excelencia en Geotermia de los Andes, CEGA", and the Millennium Science Initiative (ICM) through grant #NC130065 "Millennium Nucleus for Metal Tracing along Subduction". These projects provided funding for my scholarship, fieldwork, analyses, and the travel expenses that allowed me to present my research at various conferences. I will never be thankful enough to Bernardette Vásquez, Karin Rojas, Maritza Acuña, and Blanca Baccola, whose hard administrative work made all of this possible.

I wish to thank all my friends and colleagues from the NMTM office, for all the conversations, the laughs, the coffee, and most importantly, for sharing with me in the ups and downs of life as a graduate student. I thank Romina Gallardo, for her love, kindness, and partnership that countless times gave me the confidence to carry on with this work.

From the bottom of my heart, I thank my parents, my sister, and my grandparents, whose unconditional love, support, and dedication has allowed me to be where I am today.

Contents

List of Figures

List of Tables

CHAPTER 1: INTRODUCTION

1.1 Motivation

The Andean volcanic arc of Chile has long been recognized as one of the most promising—yet underdeveloped—geothermal provinces in the world, with estimations of geothermal energy potential varying from 3,000 to 16,000 MW for 50 years at depths of less than 3 km. (Lahsen et al., 2010; Soffia and Clavero, 2010; Aravena et al., 2016). First attempts at geothermal exploration in Chile began in the 1920s, with two wells drilled to 70–80 m depth at El Tatio Geothermal Field, although these efforts were cut short due to a lack of economic support and technical issues (Sanchez-Alfaro et al., 2015). Over the course of the remaining century, geothermal energy development in the country would see sporadic drilling and feasibility studies, focused mostly in the north (e.g. Lahsen, 1976, 1978, 1988; Cusicanqui, 1979; Letelier, 1981; Hauser, 1997). It was not until 2017, almost 100 years after the first drilling attempts, that geothermal energy in Chile would see its first success with the Cerro Pabellón Geothermal Power Plant, the first (and, as of the time of this writing, the only) geothermal power plant in South America.

One of the main obstacles to the development of geothermal energy in Chile is the critical lack of hydrogeological background knowledge on these systems. Sufficient recharge and adequate permeability pathways are essential for sustainable exploitation of the geothermal resource (Ellis and Mahon, 1977), yet there is little to no data on these parameters to support models that help evaluate sustainability of the resource at depth.

The geochemical and isotopic analysis of fluids (i.e., water and gas) can provide valuable constraints on factors such as the source of water recharge, flow-paths, residence times, and evolution of geothermal systems. Nonetheless, as hydrothermal fluids ascend towards the surface, their geochemical and isotopic signature is usually modified by shallow crustal processes, e.g., depressurization boiling, degassing, mineral precipitation, and mixing with cold groundwater in shallow aquifers (Giggenbach, 1988; Hedenquist, 1991; Arnórsson et al., 2007). These mechanisms have the potential to mask the geochemical/isotopic signature imprinted on fluids at depth, hindering interpretation of subsurface reservoir conditions. Adequately constraining these processes can significantly improve our understanding on the migration of fluids through the upper crust, and, together with the delimitation of hydrothermal system recharge, is fundamental to the development of successful geothermal exploration models.

The Lonquimay-Tolhuaca Volcanic Complex (LTVC), located in the Southern Volcanic Zone of Chile, is an area where volcanism, tectonics, hydrothermal systems, and abundant groundwater resources converge, providing an ideal setting to study these processes. The present thesis aims to understand the hydrogeochemical dynamics of the geothermal area around the LTVC, with a focus on constraining the source of groundwater recharge, identifying flow pathways, and assessing subsurface mixing rates. To accomplish this, we applied an integrated geochemical approach, including the analysis of major ion chemistry, stable isotopes (C, H, and O), and dissolved environmental tracers of anthropogenic origin (CFCs, SF_6) in thermal and cold groundwater outflowing at different localities within the LTVC.

1.2 Background

1.2.1 Geothermal systems in the Southern Volcanic Zone

Extending from the central Chilean Andes at 33°S to the Aysén Region at 46°S, the Southern Volcanic Zone (SVZ) of Chile hosts approximately one quarter of all geothermal areas in the country (Hauser, 1997; Sánchez et al., 2013). Volcanism, seismicity, and hydrothermal activity along this segment are inextricably linked (Fig. 1.1), driven by the oblique convergence between the Nazca and South American plates (e.g. Cembrano and Lara, 2009; Rosenau et al., 2006). The resulting deformation is accommodated along the intra-arc by two regional-scale fault systems: the Liquiñe-Ofqui Fault System (LOFS) and the Andean Transverse Faults (ATF). These faults are preferentially oriented and severely misoriented to the prevailing regional stress field, respectively, and exhibit contrasting characteristics with regard to permeability and fluid circulation. In recent years, significant advances have been made in deciphering the role of these structures in hydrothermal system formation, as well as unraveling their control on fluid composition (Sánchez et al., 2013; Pérez-Flores et al., 2016, 2017a,b; Tardani et al., 2016; Roquer et al., 2017; Wrage et al., 2017; Held et al., 2018).

Fracture networks of the LOFS promote infiltration of meteoric water and the development of deep convection cells. The predominant mechanism of heat transfer in these systems is thermal conduction from crystalline host rock, and the chemical composition of discharging springs is a product of heat-fluid-rock interaction at depth (Sánchez et al., 2013; Wrage et al., 2017). The ATF, in contrast, inhibit vertical fluid permeability, providing suitable conditions for the development of magma reservoirs and subsequent differentiation (Cembrano and Lara, 2009). The geochemical evolution of fluids in the ATF corresponds to meteoric water absorption of magmatic gases (leading to the formation of steam-heated reservoirs and acid-sulfate waters), and subsequent interaction with volcanic host rock (Sánchez et al., 2013; Wrage et al., 2017).

Inherent differences between these fault systems are observed in the chemical and isotopic composition of associated geothermal fluids, particularly evident in conservative element ratios such as Cl/B (Fig. 1.2), and the isotopic signature of certain volatile components (i.e. $^{3}He/^{4}He$, $\delta^{13}C\text{-}CO_2$, $\delta^{15}N$). The predominance of two clusters in geochemical data across multiple studies points to the existence of two tectonic-hydrothermal domains with different sources of mass and heat. The main geochemical characteristics of fluids in each domain are summarized in Table 1.1

On the northern termination of the LOFS, at 38°S, and along its intersection with a NW-striking fault of the ATF, lies the Lonquimay-Tolhuaca Volcanic Complex (LTVC). Lonquimay and Tolhuaca are composite stratovolcanoes of late-Pleistocene to Holocene age, with Lonquimay having recorded eruptive activity as recently as 1990. The LTVC and its surrounding area host a number of geothermal features, including natural springs, fumaroles, and boiling pools. Geothermal exploration campaigns including surface mapping, fluid chemistry analyses, resistivity (MT) measurements, and wells drilled down to ∼2000 m depth have indicated the presence of a high-enthalpy (250–300 °C) reservoir located under Tolhuaca volcano at ∼1–2 km depth (Melosh et al., 2010, 2012), yet geothermal energy capacity in the area remains unexploited. The structural arrangement of this area, including two contrast-

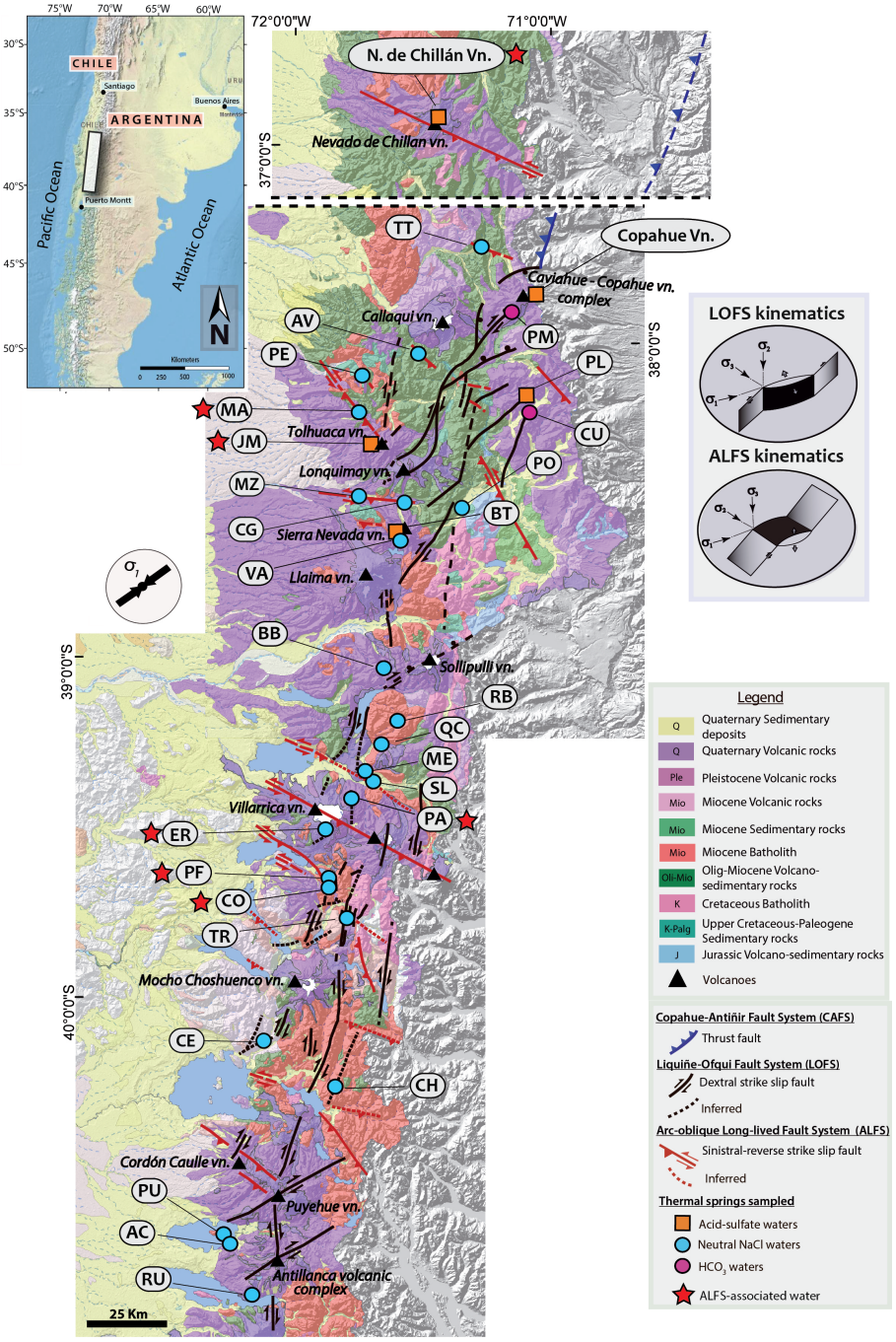

Figure 1.1: Geological map of the central segment of the SVZ (37–41°S), showing volcanoes, major fault systems with fault kinematics, and main geothermal areas classified based on predominant water type and fault association (Red star: ATF-associated, no star: LOFS-associated.) Tags indicate location name. TT: Trapa Trapa, PM: Pucón Mahuida, AV: Termas del Avellano, PE: Termas de Pemehue, PL: Pelehue, CU: Termas de Coyuco, MA: Termas de Malleco, JM: Tolhuaca Vn., MZ: Termas de Manzanar, CG: Termas de Malalcahuello, PO: Pozo de Oro (Lonquimay), BT: Sierra Nevada Vn., VA: Agua de la Vaca, BB: Termas de Balboa, RB: Termas de Río Blanco, QC: Termas Quimey-Có, ME: Parque Termal Menetúe, SL: Termas de San Luis, PA: Termas de Palguin, ER: Termas El Rincón, PF: Termas Pellaifa, CO: Termas de Coñaripe, TR: Termas de Trafipan, CH: Termas de Chihuio, PU: Termas de Puyehue, AC: Termas de Aguas Calientes, RU: Termas de Rupanco. Modified from Wrage et al. (2017)

Table 1.1: Major regional-scale geochemical differences between LOFS-associated and ATF-associated geothermal fluids.

	LOFS-associated	**ATF-associated**
Conservative elements	High Cl/B ratios (∼50).	Low Cl/B ratios (∼1).
pH	Neutral to high pH. (7–10)	Neutral to low pH (2–7).
Trace alkali metals	Strong correlation between Li, Cs, Rb and Cl (R^2: 0.7–0.9).	No correlation between trace alkali metals and Cl.
Mamgatic degassing	No direct magmatic contribution.	Meteoric water absorption of volcanic gases (CO_2, H_2S, SO_2, etc.).
Gas isotopes	Primitive isotopic signatures of volatile elements ($^3He/^4He$, $\delta^{13}C$-CO_2 , $\delta^{15}N$).	Higher degrees of crustal contamination in volatiles ($^3He/^4He$, $\delta^{13}C$-CO_2 , $\delta^{15}N$).

ing fault systems, and its hydrogeological complexity, reflected in an abundance of thermal and non-thermal manifestations, present an ideal setting to explore the effects of fracture permeability on groundwater age, fluid mixing, and dilution.

1.2.2 Groundwater age and the use of environmental tracers

The term **groundwater age** is generally 'intuitively' understood as the time elapsed between when a parcel of water first enters the saturated zone, and when it arrives at a given location (usually, the sampling point). Within this assumption, the age of a water sample corresponds to a single scalar value, with time scales ranging from a few days to thousands of years. Such an idealized parcel of water, which would be required to remain constant from the point of recharge to sampling, clearly does not exist. This highly idealized notion of groundwater age ignores the nature of molecules in a liquid, which, unlike in a solid, have more freedom to move relative to one another as they are transported. Due to the effects of molecular diffusion, hydraulic dispersion, and mixing during groundwater flow, the "neighbors" of a given water molecule in a sample will likely be very different than those it had when it originally crossed the water table, and these new neighbors may each have entered the aquifer at vastly different places and times. In other words, a single water sample can contain an entire population of unique ages. When we speak of the age of groundwater in terms of a number, we are actually referring to an unknown average of such idealized ages, known more precisely as the *apparent* age of our water sample (Suckow, 2014).

The apparent age of groundwater cannot be measured directly. It must be inferred from hydrological model simulations, or derived experimentally via the use of tracers. **Tracers**, in this context, are substances transported with groundwater that can be used to draw conclusions from the system. In very broad terms, dating with tracers consists in using a defined

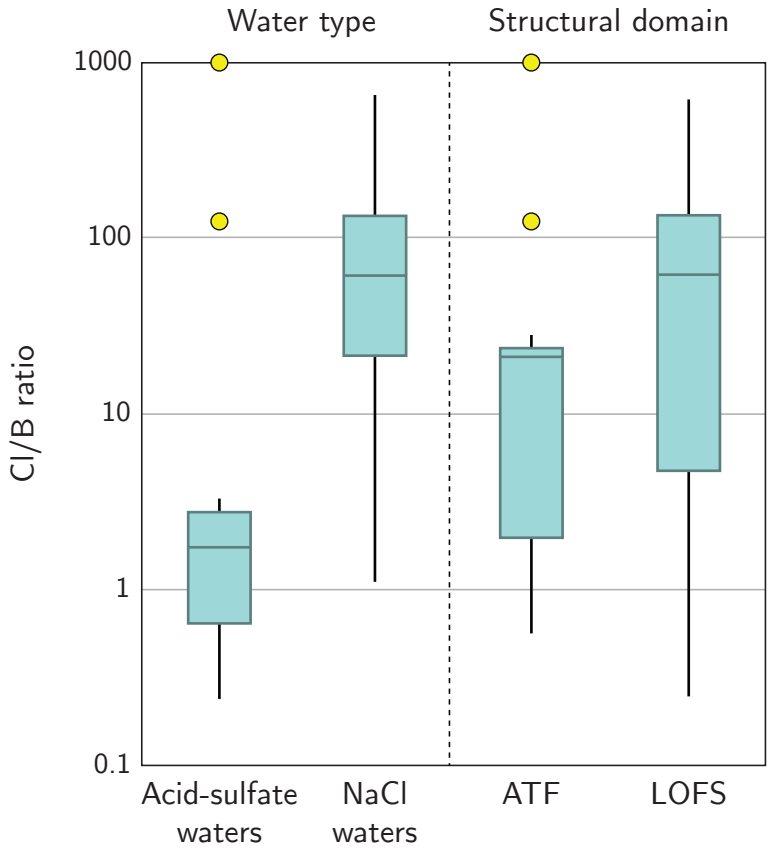

Figure 1.2: Box plot of Cl/B ratios in thermal waters of the central SVZ, according to water type (acid-sulfate vs NaCl) and fault domain (ATF vs LOFS). Yellow circles represent outliers. Modified from Wrage et al. (2017)

mathematical formula (with specific assumptions) to convert a measured tracer concentration into a model tracer age (Fig. 1.3). If we can also prove that the tracer behaves sufficiently well—that is, if it is transported with water in a sufficiently predictable manner—then the model tracer age and the apparent age of our sample will be the same. One such method employed to assess the apparent age of groundwater is the use of **environmental tracers**, such as the anthropogenic chlorofluorocarbons (CFC-12, CFC-11, CFC-113) and sulfur hexafluoride (SF_6).

CFCs and SF_6 are trace gases introduced into the Earth's atmosphere during the past century as a product of anthropogenic activities related to industrial and household applications (Maiss and Brenninkmeijer, 1998; Plummer and Busenberg, 2006). Commercial production of CFC-12 (CCl_2F_2) first began in the year 1930, followed by CFC-11 (CCl_3F) in 1936, and CFC-113 ($C_2Cl_3F_3$) in 1944 (Plummer and Busenberg, 2006). Due to their high chemical stability, low boiling points, low toxicity, and the fact that they are non-flammable and non-corrosive, these gases found extensive applications in air-conditioning and refrigeration, as solvents, blowing agents in foams, and propellants in aerosol cans, among other uses (Plummer and Busenberg, 2006). Release of these gases into the atmosphere has closely followed their production (Gamlen et al., 1986; Midgley and Fisher, 1993). CFCs are primarily responsible for the depletion of the ozone layer and are partial contributors to global warming (e.g. Molina and Rowland, 1974; Hansen et al., 1989; Kroeze and Reijnders, 1992). Atmospheric

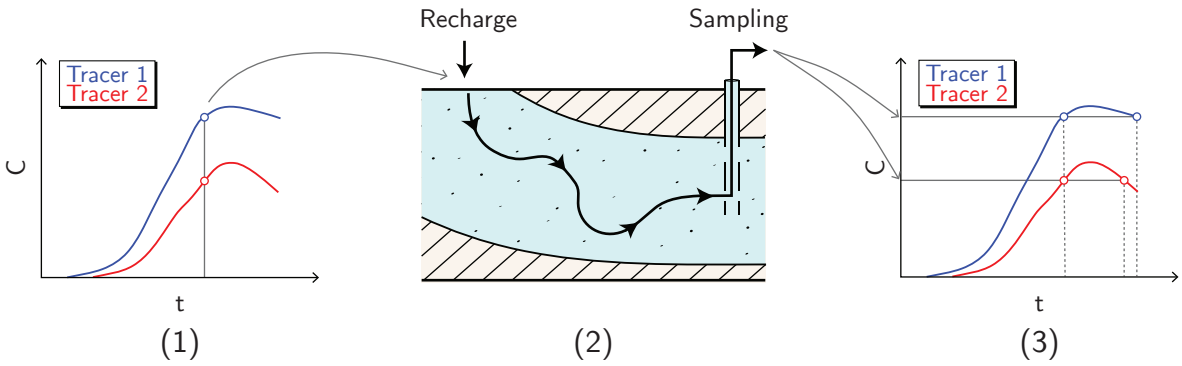

Figure 1.3: Schematic illustration showing the use of environmental tracers to characterize time-scales along a flow-path. **(1)** The concentration of a specific tracer, C, is a known function of time. When recharge occurs and the parcel of water crosses the water table, the tracer is sealed off from the atmosphere and its concentration remains fixed. **(2)** The tracer travels conservatively with water along a flow-path, from the recharge area to the point of sampling. **(3)** The dissolved tracer concentration in a water sample is measured, and used to determine the time of infiltration, t. Note that, while the conversion of time to tracer concentration is unique, the conversion of tracer concentration to time can give non-unique results. This issue can be circumvented by the use of multiple tracers.

concentrations of CFCs peaked in the 1990s, although their increase has been curtailed in the last decades due to regulations imposed by the Montreal Protocol (1987). Similarly, SF_6 is a non-flammable, non-toxic, stable gas with excellent electrical insulating properties. Production of this gas began in 1953, being used mainly as an electrical insulator in high-voltage switches and transformers (Busenberg and Plummer, 2006). SF_6 is recognized as a gas with one of the highest greenhouse warming potentials, estimated to be ~23,900 times that of CO_2 (Intergovermental Panel on Climate Change, 1995). While concentrations of CFCs have been nearly constant or decreasing in recent years, atmospheric concentrations of SF_6 have risen steadily since industrial production began in the 1950s (Maiss and Brenninkmeijer, 1998).

These gases are stable under a wide range of conditions and are water-soluble; hence, they have been incorporated into the hydrologic cycle through precipitation, infiltration, and groundwater recharge. Their concentration in the atmosphere is well established with respect to time (Elkins et al., 1993; Walker et al., 2000; Bullister, 2015), as well as the equations that characterize their solubility in water (Busenberg and Plummer, 2006; Plummer et al., 2006a), allowing their use as efficient groundwater dating tools. When compared to other environmental tracers, CFCs and SF_6 present several advantages. These gases are well-mixed in the atmosphere, meaning that their concentrations are not area-specific, unlike the more commonly used tritium (^3H). Analysis of these tracers is rapid and cost-effective compared to tritium and other radio-isotope techniques (Darling et al., 2012). Their ubiquity in the atmosphere and high chemical stability makes them suitable for dating in a wide range of environments. Of course, as with the use of any other tracer, caveats apply. Precautions must be taken to ensure that any secondary processes altering their concentrations during subsurface flow (e.g. microbial degradation, contamination, excess air, degassing, etc.) are adequately constrained (Cook et al., 2006). The solubility of these gases in water is temperature, pressure, and salinity dependent, which means that the precise inversion of tracer

concentrations to derive groundwater age depends on the accurate determination of these recharge parameters (Busenberg and Plummer, 2006; Plummer et al., 2006a).

The multi-tracer approach enables more robust groundwater dating by overcoming the limitations arising from the use of a single tracer, and reducing ambiguity in results. Secondary processes, such as degradation or contamination, can be evidenced by the elevated/reduced concentration of one tracer with respect to the others.

Outflowing springs and wells consist of several converging flow lines, each of which may likely be contributing a different apparent age to our sample (Fig. 1.4). Comparison of multiple tracers allows us to constrain mixing between end-members of different ages, and more adequately represent the age distribution of our water sample as fractions of different fluids, as opposed to the more commonly used averaged apparent age. In the context of geothermal systems, this information can be extremely useful, as it allows us to assess if deep, geothermal fluid is being diluted with modern, meteoric groundwater. This can indicate fluid mixing during ascent, or the intrusion of meteoric water into the geothermal reservoir.

1.3 Research questions and aims of this study

1.3.1 Objectives

The present thesis focuses on unraveling water recharge source, residence times, mixing, and dilution rates in the Lonquimay-Tolhuaca geothermal area of the SVZ. Our aim is to provide insights into the geochemical evolution of geothermal fluids—from infiltration to discharge—and to assess how circulation through fault-fracture networks affects the age distribution of groundwater in these systems. The main questions addressed here are:

1. What are the sources of groundwater recharge in this geothermal area?

2. Do fault-fracture meshes play a key role in thermal water circulation?

3. If so, how do these different flow mechanisms affect the residence times and mixing rates of different fluids?

1.3.2 Hypothesis

Cold groundwater and hydrothermal systems in the vicinity of the LTVC possess similar recharge sources, and the topography of the Andes plays a fundamental role in recharge distribution. Fault-fracture networks exert a primary control on geothermal fluid circulation—allowing convective flow to develop at greater depths due to the increased permeability of fractured bedrock, and acting as focused pathways for comparatively rapid vertical flux. This is reflected in the age distribution of discharging thermal springs, enabling old, deeply circulating geothermal fluid to remain relatively unmixed with young, shallow groundwater during its ascent towards the surface. In contrast, cold springs reflect shorter residence times and more complex mixing patterns, corresponding to diffuse flow through shallow permeable sediments.

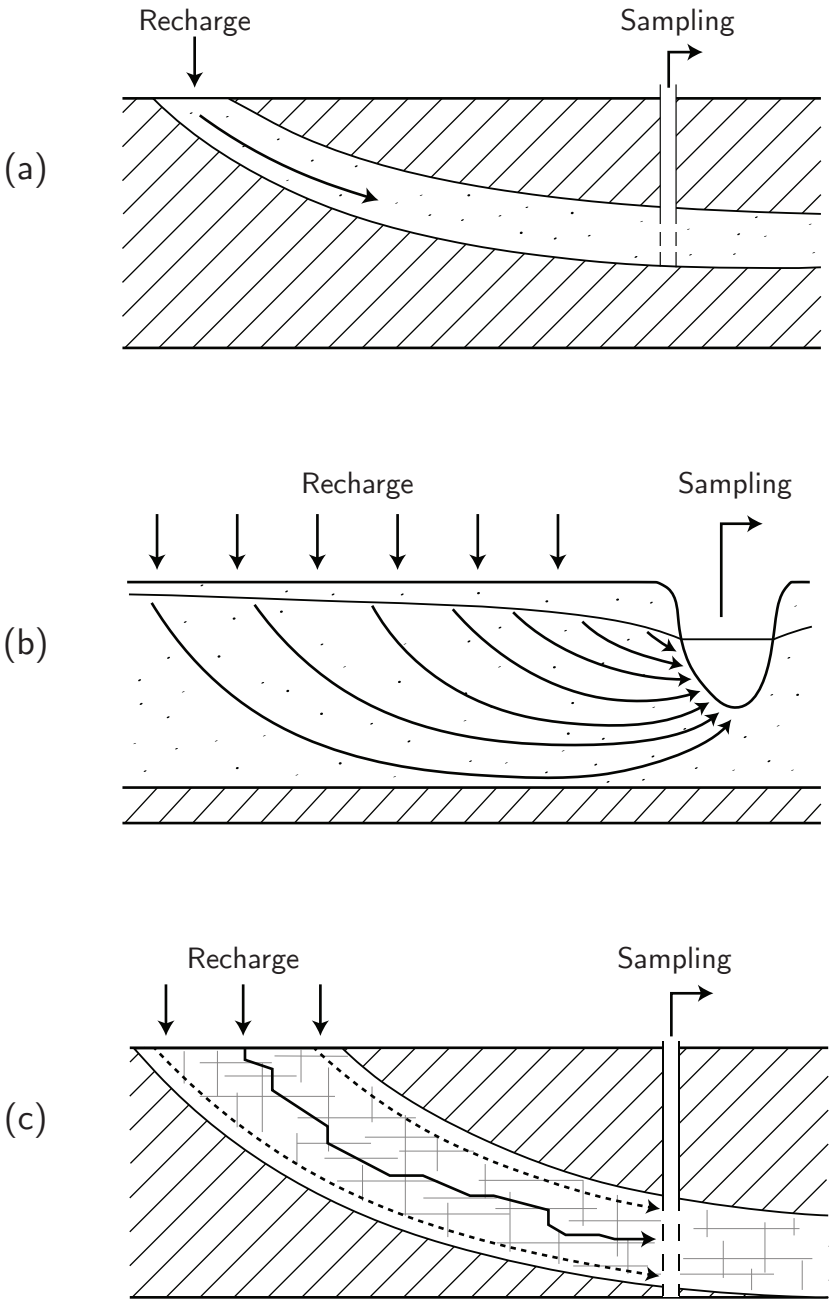

Figure 1.4: Schematic cross-section illustrating different types of groundwater flow and mixing at sampling point. **(a)** Confined aquifer with narrow recharge area. A piston flow model (PFM) is applicable if no tracer dispersion is assumed. **(b)** An unconfined aquifer with exponential distribution of transit times. If all flow lines mix at sampling point, an exponential mixing model (EMM) is applicable. **(c)** Flow along a fractured aquifer. Borehole is sampling a mixture of older, slow-moving water (dashed lines) moving through pore spaces, and young water moving rapidly through fracture networks (black line). A binary mixing model (BMM) is applicable in this situation. Modified from Małoszewski and Zuber (1982) (a,b) and Darling et al. (2012)(c).

1.4 Structure of the thesis

The present thesis is organized into three chapters. The current chapter (Chapter 1) presents a general overview of the problem, along with the research questions and aims of this study. A brief theoretical background is also provided for readers not familiar with geothermal systems in the SVZ, or the use of certain geochemical tools, such as environmental tracers for groundwater dating. Chapter 2 constitutes the central part of this dissertation, including the methodologies, results, and discussions. It is written as a self-contained paper that will be submitted for publication in an international journal upon completion of the Master's program. Chapter 3 provides a summarized review of the scientific contributions of this work and their implications, as well as a brief discussion on future work that may improve our understanding of geothermal systems in the Andes, based on the author's perspective.

In addition, supplementary material to Chapter 2 has been included for reference. Appendix A.1 contains all collected data on precipitation from the Araucanía Region, including the isotope values used for calculating the local meteoric water line. Appendix A.2 contains the PHREEQC code developed for computing the distribution of ^{13}C isotopes during CO_2 degassing and calcite precipitation in the CO_2-$CaCO_3$-H_2O system. Appendix B is a detailed description of the equations, boundary conditions, and necessary assumptions behind the Rayleigh fractionation model used to estimate recharge altitude of samples based on isotopic values.

1.5 Publications and abstracts resulting from this dissertation

Publications

Pérez-Moreno, R., Reich, M., Daniele, L., Morata, D., Held, S., Wrage, J. (2019) Stable isotope and anthropogenic tracer signature of waters in an Andean geothermal system. Manuscript in preparation. (**Chapter 2**).

Conference abstracts

Pérez-Moreno, R., Reich, M., Daniele, L., Morata, D., Tardani, D., Wrage, J., Sánchez-Alfaro, P., Held, S., Delgado, A. (2018) Constraining groundwater source and fluid-flow pathways at the Lonquimay-Tolhuaca Volcanic Complex, Southern Chile, presented at the XV Chilean Geological Congress, Concepción, Chile, November 2018.

Pérez-Moreno, R., Reich, M., Daniele, L., Morata, D., Tardani, D., Wrage, J., Sánchez-Alfaro, P., Held, S., Delgado, A. (2018) Geochemistry and environmental tracer signature of thermal waters in an Andean geothermal system, presented at Goldschmidt, Boston, MA, August 2018.

Pérez-Moreno, R., Reich, M., Daniele, L., Morata, D., Tardani, D., Wrage, J., Sánchez-Alfaro, P., Held, S., Delgado, A. (2017) Geochemical composition and anthropogenic tracer signature of thermal waters in the Lonquimay-Tolhuaca volcanic complex: Groundwater recharge source and subsurface mixing processes, presented at UNESCO IGCP636 Annual Meeting, Santiago, Chile, November 2017.

1.6 Publications resulting from side projects

Peer-reviewed

Wrage, J., Tardani, D., Reich, M., Daniele, L., Arancibia, G., Cembrano, J., Sánchez-Alfaro, P., Morata, D., **Pérez-Moreno, R**. (2017). Geochemistry of thermal waters in the Southern Volcanic Zone, Chile – Implications for structural controls on geothermal fluid composition. *Chemical Geology*, 466:545–561, doi:10.1016/j.chemgeo.2017.07.004.

Other publications

Alvial, I.*, Johansson, C.*, More, J.*, Neirot, A.*, **Pérez-Moreno, R.***, Retamal, A.*, Rivera, J.*, Rodríguez, F.*, Toledo, P.*, Garretón, V., Hevia, S., Roberts, R., González, P. (2018). *El agua como recurso vital* [Water as a vital resource], published by the Library of National Congress of Chile and the Millennium Science Initiative. Available at: iniciativamilenio.cl/legislacion.

* Indicates equally contributing authors, listed in alphabetical order.

CHAPTER 2: STABLE ISOTOPE AND ANTHROPOGENIC TRACER SIGNATURE OF WATERS IN AN ANDEAN GEOTHERMAL SYSTEM

Rodrigo Pérez-Moreno [a,b,*], Martin Reich [a,b], Linda Daniele [a,b], Diego Morata [a,b], Sebastian Held [c], Jackie Wrage [d]

[a] *Department of Geology and Andean Geothermal Center of Excellence (CEGA), FCFM, Universidad de Chile, Plaza Ercilla 803, Santiago, Chile*

[b] *Millennium Nucleus for Metal Tracing Along Subduction, FCFM, Universidad de Chile, Santiago, Chile*

[c] *Institute of Applied Geosciences, Karlsruhe Institute of Technology (KIT), Karlsruhe, Germany*

[d] *Department of Geological Sciences, University of Michigan, Ann Arbor, MI, USA*

* Corresponding author at: Department of Geology and Andean Geothermal Center of Excellence (CEGA), FCFM, Plaza Ercilla 803, Santiago, Chile.
E-mail address: rodrigoperez@ug.uchile.cl (R. Pérez-Moreno).

Keywords: Geothermal systems; Geochemical modeling; Stable isotopes; Anthropogenic tracers; Chlorofluorocarbons; Sulfur hexafluoride; Southern Volcanic Zone (SVZ)

ABSTRACT

In the present study, we combined stable isotopes and anthropogenic tracers to investigate the origin, residence times, and evolution of thermal waters in the Lonquimay-Tolhuaca Volcanic Complex (LTVC) of the southern Chilean Andes. A total of 20 groundwater samples from springs discharging at a broad range of temperatures (8–96°C) were collected and analyzed for major ion geochemistry, stable isotope ratios (δ^2H, δ^{18}O, $\delta^{13}C_{TDIC}$), dissolved chlorofluorocarbons (CFCs) and sulfur hexafluoride (SF_6). In addition, we compiled all available data on the isotopic composition of precipitation in the region to derive the local meteoric water line. Coupled with a Rayleigh-fractionation model of precipitation, we provide constraints on the elevation at which infiltration and recharge to the system is produced. δ^{13}C values are consistent with the bulk of dissolved inorganic carbon being derived from the addition of soil CO_2 to an atmospheric source, while magma degassing and boiling processes are evidenced in samples discharging directly on the flanks of volcanoes. The isotopic composition of thermal water, once heated at depth, is further modified by CO_2 degassing and carbonate precipitation during ascent. All geothermal samples contain low but detectable concentrations of CFC-11, CFC-12, CFC-113 and SF_6, suggesting the addition of only a small fraction (2 to 22%) of modern meteoric water. The discharge temperature

of naturally outflowing springs in the LTVC correlates directly with the age distribution of the water samples. This difference in residence times is attributed to the distinct subsurface circulation pathways of each water type—i.e., the shallow, diffuse flow of cold groundwater vs. the deep, focused circulation of thermal water along fault zones. Conduit flow along high vertical permeability networks allows hydrothermal fluid to remain relatively unmixed with shallow meteoric water during ascent. Data from this study confirm that fault-fracture meshes with different orientations exert a first order control on the residence times, ascent, and mixing rates of thermal waters in this segment of the Andean Cordillera, thus modulating their chemical and isotopic signature. Additionally, our results show that the combined use of conventional hydrogeochemical and isotopic data with environmental tracers, including anthropogenic CFCs and SF_6, is a powerful tool to better understand the dynamics of geothermal systems.

2.1 Introduction

There is a general agreement that fault-fracture networks play a fundamental role on permeability distribution in the crust (e.g. Sibson, 1996; Manning and Ingebritsen, 1999; Rowland and Sibson, 2004; Faulkner et al., 2010). This, in turn, affects residence times, water-rock ratios, and mixing rates, ultimately impacting the geochemical composition of the circulating fluid. For example, in the Southern Andean Volcanic Zone (SVZ) of Chile, significant advances have been made in constraining the role of fault-fracture meshes on hydrothermal system formation (Sánchez et al., 2013; Pérez-Flores et al., 2016; Tardani et al., 2016; Roquer et al., 2017; Wrage et al., 2017). Orientation with respect to the prevailing stress field, dictated by the tectonic regime, impacts fault and fracture aperture and may play a significant role in either facilitating or hindering fluid circulation (Pérez-Flores et al., 2017b). Favorably oriented structures can act as high-flux vertical conduits for hydrothermal fluid, promoting deep convection cells and fluid-rock interaction at depth. In contrast, inherited basement faults, strongly misoriented with respect to the present-day stress regime, form compressional structures that favor magma emplacement in the crust. This leads to increased reservoir temperatures and deep-crust/mantle contributions through magmatic degassing (Ray et al., 2009; Tardani et al., 2016), imparting a distinct geochemical signature on hydrothermal fluid depending on the associated volcano-tectonic domain (Sánchez et al., 2013; Wrage et al., 2017).

Nonetheless, as hydrothermal fluids ascend towards the surface, their geochemical and isotopic signature is usually modified by shallow crustal processes such as depressurization boiling, degassing, mineral precipitation, and mixing with cold groundwater in shallow aquifers (Giggenbach, 1988; Hedenquist, 1991; Arnórsson, 1995; Arnórsson et al., 2007; Kaasalainen and Stefánsson, 2012). These mechanisms usually occur in conjunction with one another, and can potentially mask the geochemical/isotopic signature imprinted on the fluid at depth, hindering interpretation of subsurface reservoir conditions. Adequately constraining these processes can significantly improve our understanding fluid migration through the crust, and, together with the delimitation of hydrothermal system recharge, is fundamental to the development of successful geothermal exploration models.

The present study focuses on unraveling water recharge source, residence times, fluid mixing, and dilution rates in the Lonquimay-Tolhuaca geothermal area of the SVZ. Our aim is to provide insights into the geochemical evolution of geothermal fluids, from infiltration to discharge, and to assess how circulation through fault-fracture networks affects the residence times and mixing rates of groundwater in these systems.

The area surrounding the Lonquimay-Tolhuaca Volcanic Complex (LTVC) in the southern Andes of Chile (38°S) hosts several geothermal surface manifestations, including fumaroles, thermal springs, and bubbling pools. Within this area, geothermal activity occurs in close spatial relationship with two major tectonic features: the NNE to NE-trending Liquiñe-Ofqui Fault System (LOFS) and the WNW-striking Andean Transverse Faults (ATF) (Lopez-Escobar et al., 1995; Lara et al., 2006; Cembrano and Lara, 2009; Sánchez et al., 2013). The complex interplay between these contrasting fault systems and geothermal activity presents an ideal setting to explore the effects of fracture permeability on hydrothermal fluid circulation. To accomplish this, we apply an integrated geochemical approach—including the analysis of major ion chemistry, stable isotopes (C, H, and O), and dissolved environmental tracers of anthropogenic origin (CFCs, SF_6)—in thermal and cold groundwater outflowing at different localities within the LTVC.

Oxygen and hydrogen isotopes are proven tracers for establishing recharge areas in regions with significant elevation changes, such as the Andean Cordillera (e.g. Dansgaard, 1964; Clark and Fritz, 1997; James et al., 2000; Rowley, 2007). Similarly, stable isotopes of dissolved carbon can provide information on fluid source(s) and other fundamental processes commonly occurring in hydrothermal settings, such as CO_2 degassing and carbonate precipitation (Rose and Davisson, 1996; Chiodini et al., 2000; Frondini et al., 2009). Chlorofluorocarbons (CFCs) and sulfur hexafluoride (SF_6) are trace gases introduced into the Earth's atmosphere during the past century as a product of anthropogenic activities related to industrial and household applications (Maiss and Brenninkmeijer, 1998; Plummer and Busenberg, 2006). CFCs are primarily responsible for the depletion of the ozone layer and are partial contributors to global warming (e.g. Molina and Rowland, 1974; Hansen et al., 1989; Kroeze and Reijnders, 1992). These gases are stable under a wide range of conditions and are water-soluble; hence, they have been incorporated into the hydrologic cycle through precipitation, infiltration, and groundwater recharge. Their concentration in the atmosphere is well established with respect to time (Elkins et al., 1993; Walker et al., 2000; Bullister, 2015), as well as the equations that characterize their solubility in water (Busenberg and Plummer, 2006; Plummer et al., 2006a), allowing their use as efficient groundwater dating tools. These tracers serve as extremely sensitive indicators of the presence of a 'modern' (>1940) groundwater component. Furthermore, the analysis of multiple tracers allows us to compare tracer ratios and elucidate mixing between waters of different ages. Based on our combined geochemical, stable isotope, and anthropogenic tracer results, we propose a hydrogeochemical model for fluid circulation consistent with the structural arrangement of the SVZ.

2.2 Geological background

2.2.1 Regional tectonic and structural setting

The tectonic and structural setting of the Southern Volcanic Zone (SVZ) of Chile is driven by oblique convergence between the Nazca and South American plates at a rate of ca. 6.6 cm/year (Pardo-Casas and Molnar, 1987; Somoza, 1998; Angermann et al., 1999). The resulting dextral transpressional strike-slip-dominated deformation is partially accommodated along the intra-arc by two major tectonic features, which are ubiquitous throughout the SVZ: the Liquiñe-Ofqui Fault System (LOFS) and the Andean Transverse Faults (ATF). The LOFS is a 1200-km-long major fault system present between 38°S and 47°S (Cembrano et al., 1996; Rosenau et al., 2006; Cembrano and Lara, 2009). It is composed of a series of subvertical, NNE-striking dextral-shearing master faults, second order subvertical NE to ENE-striking normal faults which splay off these master faults, and third order ENE-to-EW striking faults (Pérez-Flores et al., 2017b). In contrast, the ATF are a series of discrete, steeply-dipping WNW-striking faults which are severely misoriented for shear with respect to the prevailing stress field, and thus require supralithostatic fluid pressures to become active (Pérez-Flores et al., 2016; Sanchez-Alfaro et al., 2016; Roquer et al., 2017). The ATF have been interpreted as crustal weaknesses associated with pre-Andean faults that reactivated as sinistral-reverse strike-slip faults during arc development (Lopez-Escobar et al., 1995; Lara et al., 2006; Melnick et al., 2006; Pérez-Flores et al., 2016). These transverse faults play a major role in the formation of volcanic systems (e.g. Lonquimay-Tolhuaca volcanic complex, Villarrica-Quetrupillan-Lanín volcanic chain) as they provide suitable conditions for the development of magma reservoirs and subsequent differentiation (Cembrano and Lara, 2009), as well as long-lived potential pathways for crustal ascent of deep-seated fluids (Pérez-Flores et al., 2016; Sanchez-Alfaro et al., 2016; Tardani et al., 2016).

The area of the Lonquimay-Tolhuaca Volcanic Complex, which is the focus of the present investigation, is located in the northern termination of the LOFS, roughly near 38°S (Fig. 2.1). In this area, master and subsidiary faults of the LOFS splay off to the NE, forming duplex and horsetail geometries. This eastward shift in strike develops extensional and hybrid (extension + shear) cracks, which constitute localized permeability pathways that may enhance the vertical migration of fluids in the crust (Melnick et al., 2006; Sánchez et al., 2013; Pérez-Flores et al., 2016; Roquer et al., 2017; Wrage et al., 2017).

2.2.2 Subsurface geology and geothermal reservoir potential

The Cura-Mallín basin developed as an intra-arc basin of the upper Oligocene-lower Miocene volcanic arc between 36° to 39°S (Niemeyer and Muñoz, 1983; Suárez and Emparan, 1997). The infill is comprised of the Cura-Mallín Group (re-defined as such by Pedroza et al. (2017), previously the *Cura-Mallín Formation*), with an estimated thickness of 2–4 km (Burns et al., 2006; Radic, 2010). In the study area, the Cura-Mallín Group is divided into two roughly contemporaneous (22—11 Ma), but lithologically distinct formations which interdigitate with one another at the base: The volcano-sedimentary Guapitrío Formation

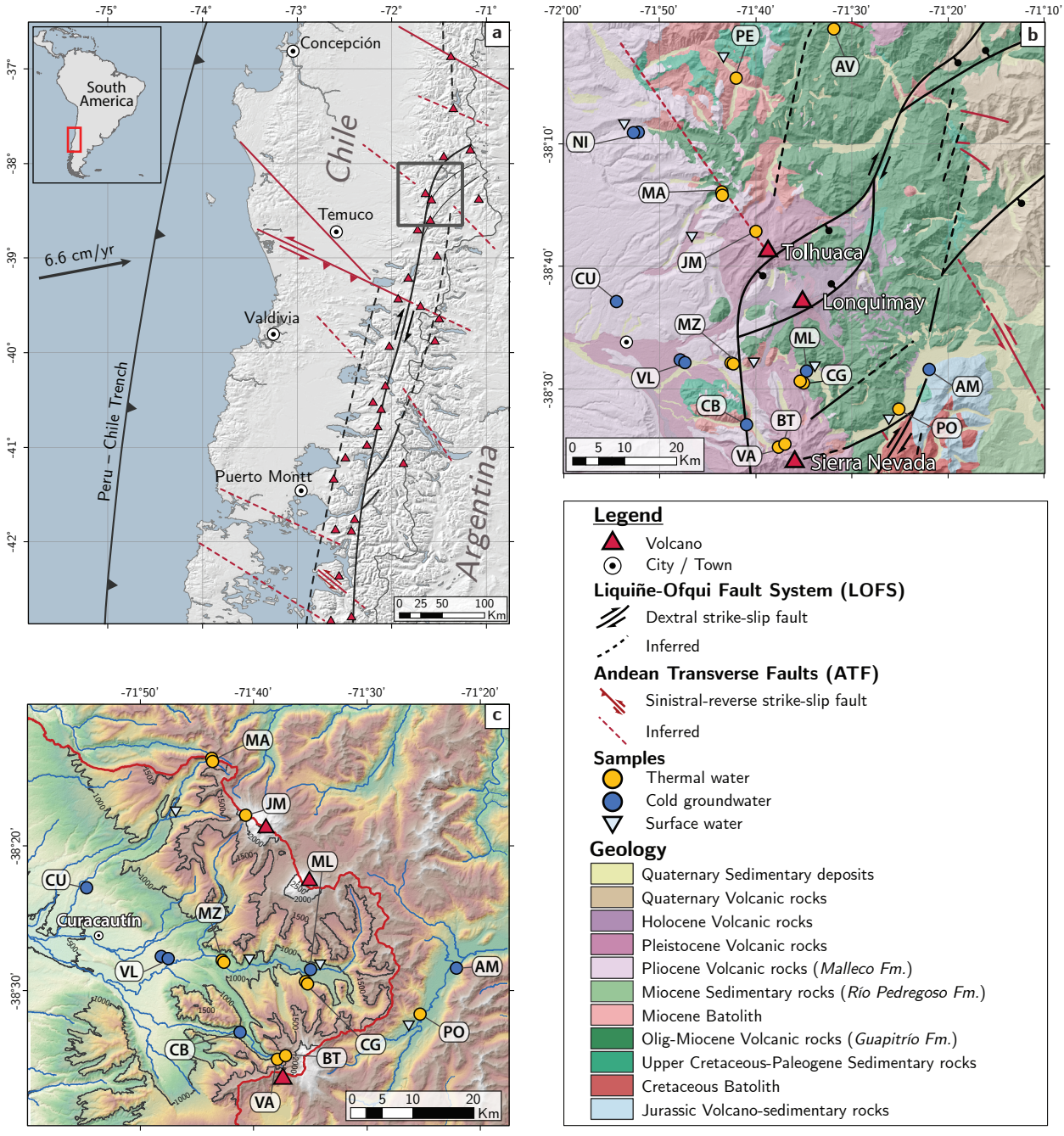

Figure 2.1: Map of the study area. **(a)** Structural map of the Central Southern Volcanic Zone (37° to 41.5°S), showing the trench and convergence vector (Angermann et al., 1999), Liquiñe-Ofqui Fault System (black lines), Andean Transverse Faults (red lines), and genetically associated volcanoes. Black square marks the study area. **(b)** Geological-structural map of the Lonquimay-Tolhuaca Volcanic Complex, located at the northern termination of the LOFS. Structures from Pérez-Flores et al. (2016). Samples are shown with their respective location ID. **(c)** Hydrology of the southern LTVC. Red curve represents the water divide delimiting the Río Imperial basin. Blue lines are drainage networks. Contour lines show elevation in m a.s.l.

and the sedimentary Río Pedregoso Formation (Pedroza et al., 2017). The Guapitrío Fm. hosts a fossil hydrothermal system outcropping east of the LTVC, and is considered to be of low potential for present-day convective fluid flow, due to extensive hydrothermal alteration that produced secondary minerals clogging pore spaces and fractures (Suárez and Emparan, 1997; Vicencio, 2015; Pedroza et al., 2017). The sedimentary Río Pedregoso Fm. has grain sizes that range from impermeable shales and mudstones, to relatively thick, semi-permeable sandstones and conglomerates which may have sufficient primary permeability for geothermal reservoirs to develop at depth (Suárez and Emparan, 1997; Pedroza et al., 2017). To the west, the volcanic Pliocene-Pleistocene (4–1 Ma) Malleco Formation overlies the Cura-Mallín Group in unconformity (Suárez and Emparan, 1997). Batholitic rocks of Miocene age intrude these units and outcrop to the north and south of the LTVC.

The above described units constitute the basement underlying a series of Quaternary volcanoes and are potential host units for geothermal reservoirs. Permeability in sandstones of the Río Pedregoso Fm. ranges from 10^{-1} m^2 (semi-permeable) to 10^{-6} m^2 (almost impermeable) (Pedroza et al., 2017). Representative samples of volcanic and plutonic rocks in the study area have baseline values that range from 10^{-18} to 10^{-20} m^2, though it has been observed that the presence of throughgoing mated macro-fractures can increase permeability of these rocks by four to six orders of magnitude, which would allow convective flow to develop (Pérez-Flores et al., 2017a). These enhanced values are more consistent with those that allow hydrothermal convection of heated groundwater to form in the crust ($> 10^{-16}$ m^2) (Cathles et al., 1997).

2.2.3 Climate of the study area and groundwater occurrence

Moisture in the western slopes of the southern Andes is derived as precipitation from the Pacific, and carried inland by the Southern Hemisphere westerly winds. In this area, orography plays an important role on climate and precipitation distribution (e.g. Seluchi et al., 1998; Garreaud, 2009; Insel et al., 2010). The dominant mechanisms that control the amount of precipitation and its isotopic composition are the orographic uplift of air and seasonal variations in temperature (Stöwhas and Moyano, 1993; Rozanski and Araguás-Araguás, 1995). Climate of the study area is characterized by mild temperatures during the summer months (∼16°C) and cold winters (∼8°C). Mean annual precipitation exceeds 2000 mm per year, being lowest in January (∼50–70 mm) and highest in June (> 300 mm) (data collected from the CR2 database, http://explorador.cr2.cl). Streamflow records from 1940 onwards indicate that the hydrological regime in this region is fundamentally pluvial with a small snowmelt contribution during spring (Fernández et al., 2018).

2.3 Sampling and analytical techniques

A total of 20 groundwater samples from naturally discharging springs and 6 surface water samples were collected within the period of 2016–2018 and analyzed for major element geochemistry at the Andean Geothermal Center of Excellence (CEGA) Laboratories, University

of Chile, in Santiago, Chile. During sampling, outflow temperature, pH, conductivity and redox potential were measured using a Hach HQ-40 multiparameter probe. Samples were filtered through a 0.45 µm filter (cellulose acetate) into pre-cleaned high-density polythene bottles with double caps. Samples for major cation analysis were acidified with HNO_3 (Merck Suprapur) 4N, 1 mL to 100 mL sample. Cations were analyzed by ICP-OES (Optima 7300V, Perkin Elmer). Anions were measured by ion chromatography (Dionex ICS-2100, Thermo-Scientific). Carbonate alkalinity (HCO_3^- and CO_3^{2-}) was measured using the volumetric titration methods described in Giggenbach and Gougel (1989). SiO_2 contents were analyzed by Portable Photometer (Hanna HI96705). Total dissolved inorganic carbon (TDIC) and saturation indices of select minerals were calculated for each sample using the aqueous speciation model program PHREEQC and the Lawrence Livemore National Laboratory database (Parkhurst and Appelo, 2013)

Samples were analyzed for δ^2H, $\delta^{18}O$ (V-SMOW), and $\delta^{13}C_{TDIC}$ (PDB) at the University of Waterloo Environmental Isotope Laboratory. Samples were collected in 125 mL high-density polythene bottles, double capped and avoiding any headspace. Vials for carbon isotope analyses were preserved with a few drops of $HgCl_2$ to prevent fractionation due to biological activity. Samples were kept refrigerated at 4°C prior to being shipped for analysis. $^{18}O/^{16}O$ and $^2H/^1H$ ratios were analyzed by Off-Axis Integrated Cavity Output Spectroscopy (OA-ICOS) laser absorption using a Los Gatos Research Liquid Water Isotope Analyzer, model T-LWIA-45-EP with precisions of $\delta^2H = \pm 0.8‰$ and $\delta^{18}O = \pm 0.2‰$. $^{13}C/^{12}C$ ratios were analyzed by a Micromass-IsoPrime mass spectrometer. Precision of analyses was $\delta^{13}C = \pm 0.2‰$. Samples AV(1), PE(2), CG(15), CG(16), and R1(21) were analyzed for δ^2H and $\delta^{18}O$, and $\delta^{13}C$ in the Laboratory of Biogeochemistry of Stable Isotopes at the Andalusian Institute of Earth Sciences (CSIC, Spain) using a Finnigan Delta Plus XL mass spectrometer attached to a Finnigan GasBench II, with an analytical error of ± 1.1‰, ± 0.1‰, and ± 0.05‰ respectively.

In order to determine groundwater age and constrain possible subsurface mixing processes, concentration of dissolved anthropogenic tracers chlorofluorocarbons (CFC-11, CFC-12, CFC-113) and sulfur hexafluoride (SF_6) was measured. Sampling procedures for these tracers followed guidelines described in Busenberg et al. (2006). Springs were sampled using a peristaltic pump fitted with Viton tubing, with one end of the tube inserted at the bottom of the sampling vial and the other in the opening of the spring where maximum discharge occurred. Viton is the only elastomer adequate for use in pumps that does not contaminate the sample due to diffusion of CFCs into the polymer and subsequent release into the water (Reynolds et al., 1990; Cook et al., 2006). Samples were collected in 1 L glass bottles with metal lined caps and enclosed in tight copper tins to prevent atmospheric contamination. Bottles were placed on a 10 L bucket and filled from the bottom up. The bucket was allowed to overflow by at least three bottle volumes before capping bottles and tins underwater. All materials were flushed extensively with sample water prior to collection. When atmospheric contamination could not be excluded due to unfavorable outflow conditions, springs were not sampled. CFCs and SF_6 were analyzed by purge and trap gas chromatography with an electron capture detector (Bullister and Weiss, 1988; Happell et al., 1996) at the *Spurenstofflabor*, Wachenheim, Germany. The detection limit for CFCs was 0.01 pmol kg^{-1} and 0.1 fmol kg^{-1} for SF_6.

2.4 Results

Table 2.1 presents the analytical results (physicochemical parameters, chemical composition, stable isotope signature, and anthropogenic tracer concentration) of water samples from this study, as well as physicochemical parameters measured *in situ*. The data set includes 12 samples which were classified as thermal (Discharge temperature > Air temperature + 4°C), 8 cold groundwater samples (Discharge temperature < Air temperature + 4°C) and 6 surface water samples corresponding to major perennial rivers in the study area. Samples are sorted in latitudinal order from north to south and with an ID label corresponding to sampling location. In locations with more than one discharge point, samples were selected for anthropogenic tracer analysis (CFCs, SF_6) based on best outflow conditions. Fig. 2.1b shows all sample locations.

2.4.1 Physicochemical parameters and fluid chemistry

Thermal waters in the study area discharge at a broad range of temperatures (31° to 96 °C), pH (2.4 to 9.8), and total dissolved solids (111 to 2805 mg L^{-1}). Samples were classified based on major ion concentrations. All thermal waters classified as Na-Cl waters, with the exception of two high temperature, high sulfate springs (JM(7) and BT(19)), located near zones of fumarole activity, which classified as Ca-SO_4 waters. Na-Cl waters tend to cluster in the Na + K corner of the ternary cation plot and are dispersed throughout the ternary anion plot, while calcium-sulfate waters fall near the SO_4^- corner of the anion plot and have higher relative concentrations of Ca and Mg. (For a comprehensive discussion of the major ion geochemistry of thermal waters in the SVZ, as well as the formation mechanisms involved behind each water type, the reader is referred to Wrage et al. (2017).)

In contrast to thermal springs, cold groundwaters exhibit more narrow ranges, with temperatures from 8 to 13 °C, a more neutral pH (5.5 to 7.9) and a more dilute composition (40 to 284 mg L^{-1}). These parameters are more akin to those observed in surface waters (pH 6.7–7.6, TDS 35–96 mg L^{-1}). Cold groundwaters and surface water samples all classified as bicarbonate waters. Figure 2.2 illustrates the major cation and anion composition of all samples, showcasing the distinct chemical composition of hot and cold groundwaters.

2.4.2 Stable isotope composition

$\delta^{18}O$ and δ^2H

Figure 2.3 shows the δ^{18}O and δ^2H values of groundwater and surface water samples. With the exception of the two sulfate waters identified in the previous section (JM(7) & BT(19)), the oxygen and hydrogen isotope signatures of hot, cold and surface samples present no major differences in overall composition (δ^{18}O: thermal waters −11.5 to −8.9‰, cold groundwater −11.6 to −8‰, surface waters −10.1 to −8.6‰; δ^2H: thermal waters −78.11 to −61.2‰, cold groundwater −82.7 to −57.98‰, surface waters −68.7 to −59.1‰). To supplement

Table 2.1: Chemical composition, isotopic signature, and atmospheric tracer concentration of water samples in the study area.

#	ID	Location name	Sample type	Location* Easting	Location* Northing	Temp. [°C]	pH	Eh [mV]	TDS [mg/L]	SiO_2 [mg/L]	Na [mg/L]	K [mg/L]	Ca [mg/L]	Mg [mg/L]
1	AV	Termas del Avellano	Thermal	277623	5792326	67.8	8.1	-25.5	768	97	198.0	9.75	25.60	0.179
2	PE	Termas de Pemehue	Thermal	263072	5782280	36.1	7.8	334.8	2805	94	793.0	38.40	153.00	0.414
3	NI	Niblinto	Cold	248525	5773548	11.8	5.5	363.6	49	14	2.5	<0.4	3.61	1.575
4	NI	Niblinto	Cold	247743	5773517	10.4	6.3	412.4	49	19	2.4	0.44	3.13	1.160
5	MA	Termas de Malleco	Thermal	261523	5764434	84.6	8.3	-207.1	447	158	102.0	4.27	5.59	0.050
6	MA	R.N. Malleco	Thermal	261451	5765257	30.8	8.8	-114.6	111	29	22.9	<0.4	4.53	0.235
7†	JM	Tolhuaca Vn.	Thermal	266696	5758625	92.0	2.4	n.a.	798	82	17.3	5.20	31.40	16.000
8	CU	Curacautín	Cold	245946	5747882	11.0	5.7	394.0	41	16	2.5	1.07	2.61	0.790
9	VL	Vega Larga	Cold	256658	5739110	9.7	7.3	428.3	129	30	7.9	1.54	9.84	5.200
10	VL	Vega Larga	Cold	255768	5739368	13.2	6.2	420.0	88	24	6.6	0.90	6.07	2.180
11	MZ	Manzanar	Thermal	263738	5739080	45.4	9.7	290.5	250	67	70.0	1.00	1.25	0.022
12	MZ	Manzanar	Thermal	263715	5739024	48.2	9.6	45.3	251	63	70.0	0.92	1.12	0.004
13	AM	Agua del mote	Cold	293689	5738927	11.3	7.8	28.8	286	31	24.6	1.35	40.40	3.900
14	ML	Malalcahuello	Cold	274910	5738246	8.4	7.9	396.5	88	24	5.4	0.69	9.56	1.450
15	CG	Casagrande	Thermal	274480	5736573	40.5	9.3	277.3	200	50	49.9	0.94	2.68	0.001
16	CG	Casagrande	Thermal	274480	5736573	40.2	9.5	315.2	180	48	43.5	0.81	3.14	0.009
17	PO	Pozo de Oro	Thermal	289182	5732951	32.7	9.0	385.5	440	40	117.0	1.18	15.00	0.118
18	CB	Cañón del Blanco	Cold	266164	5729992	12.0	7.3	391.5	139	37	13.1	2.76	13.30	3.480
19	BT	Baños del Toro	Thermal	272137	5727180	95.7	7.0	n.a.	380	83.1	24.2	3.12	88.62	6.279
20	VA	Agua de la Vaca	Thermal	271097	5726641	63.2	7.1	269.4	965	145	179.0	24.24	65.40	3.368
		Surface waters												
21	R1	Diablo River	Surface	261107	5784738	6.2	7.2	455.4	42	10	2.4	0.31	5.01	0.660
22	R2	Niblinto River	Surface	246313	5773972	9.4	6.6	342.6	35	11	2.1	<0.40	3.18	0.686
23	R3	Corcoludo River	Surface	257035	5757208	3.8	6.7	421.4	38	17	2.3	0.61	2.07	0.700
24	R4	Cautín River	Surface	263718	5739092	9.1	7.6	341.7	96	29	6.2	1.15	8.71	2.870
25	R5	Cautín River	Surface	275023	5737727	7.5	6.7	346.4	63	23	3.2	0.69	4.44	1.425
26	R6	Punta Negra River	Surface	287742	5730775	8.8	6.9	379.5	36	13	1.8	0.41	2.80	0.772

n.a = not analyzed; n.d = not detected (sample concentration below detection limit); E_h is given relative to the standard hydrogen electrode.

* WGS84/UTM zone 19S

† Geochemical and isotope data from Wrage et al. (2017)

Table 2.1: (continued)

#	ID	F [mg/L]	Cl [mg/L]	SO_4 [mg/L]	Br [mg/L]	NO_3 [mg/L]	PO_4 [mg/L]	HCO_3 [mg/L]	CO_3 [mg/L]	δ^2H [‰]	$\delta^{18}O$ [‰]	TDIC [mmol/kg]	$\delta^{13}C_{TDIC}$ [‰]	SI Calcite	SI Dolomite
1	AV	2.04	233.0	167.0	0.28	0.77	<0.1	34.2	n.d.	-66.8	-9.7	0.431	-14.9	-0.01	-0.73
2	PE	2.69	1436.0	259.0	4.21	0.12	<0.1	24.3	n.d.	-61.2	-8.9	0.363	-13.3	-0.20	-1.53
3	NI	<0.03	1.2	0.5	<0.05	3.07	<0.2	22.9	n.d.	-58.0	-8.0	3.693	-19.9	-4.06	-7.16
4	NI	<0.03	0.8	0.6	<0.05	<0.1	<0.2	22.2	n.d.	-58.1	-8.3	0.884	-20.0	-3.36	-5.84
5	MA	2.11	37.1	25.2	0.10	0.49	<0.1	112.0	n.d.	-65.8	-9.7	1.413	-9.2	0.34	0.23
6	MA	0.29	7.1	17.4	<0.05	<0.1	<0.2	27.0	3.5	-66.2	-9.9	0.489	-15.0	-0.33	-0.52
7†	JM	0.12	0.5	645.0	n.d.	n.d.	n.d.	n.d	n.d.	-45.7	-5.3	n.a.	n.a.	n.a.	n.a.
8	CU	<0.03	2.2	0.3	<0.05	0.46	<0.2	15.2	n.d.	-59.8	-8.6	1.666	-20.3	-4.19	-7.57
9	VL	0.04	2.5	14.8	<0.05	0.38	<0.2	56.0	n.d.	-70.8	-10.2	1.046	-5.1	-1.53	-2.03
10	VL	<0.03	3.0	7.5	<0.05	6.81	<0.2	31.1	n.d.	-62.2	-9.1	1.370	-17.2	-3.01	-5.13
11	MZ	1.22	17.8	47.0	<0.03	0.36	0.25	41.8	2.3	-64.0	-9.7	0.724	-14.1	-1.29	-2.87
12	MZ	1.25	18.7	49.1	<0.03	0.26	0.25	42.4	3.5	-64.0	-9.9	0.753	-11.2	-1.03	-3.03
13	AM	0.14	2.3	18.8	<0.05	1.49	<0.2	161.6	n.d.	-82.7	-11.6	2.744	-14.8	0.01	0.32
14	ML	0.05	1.1	1.2	<0.05	0.80	<0.2	43.2	n.d.	-70.4	-9.8	0.729	-15.5	-1.05	-1.62
15	CG	0.85	15.0	47.1	0.04	0.66	<0.1	33.3	<1.0	-65.8	-10.4	0.208	-16.1	-0.38	-2.74
16	CG	0.64	11.4	37.4	<0.03	0.44	<0.1	32.9	1.7	-67.4	-10.1	0.153	-17.4	-0.27	-1.63
17	PO	0.91	73.1	171.0	0.18	0.15	<0.1	21.8	<1.0	-78.1	-11.2	0.214	-16.5	-0.10	-0.92
18	CB	0.07	12.6	15.8	0.05	0.13	<0.2	40.9	n.d.	-64.0	-9.5	0.759	-15.3	-1.50	-2.26
19	BT	n.a.	0.3	232.0	n.a.	n.a.	n.a.	106.8	n.d.	-54.5	-7.1	n.a.	n.a.	n.a.	n.a.
20	VA	0.34	279.0	186.0	0.75	0.45	<0.1	81.9	n.d.	-67.0	-9.5	1.490	-9.8	-0.18	-0.20
Surface waters															
21	R1	<0.03	1.5	2.6	<0.03	0.75	<0.1	19.3	n.d.	-64.8	-9.4	0.378	-8.4	-2.39	-4.38
22	R2	<0.03	0.7	2.8	<0.05	<0.1	<0.2	14.5	n.d.	-59.1	-8.6	0.412	-5.1	-3.25	-5.86
23	R3	<0.03	0.9	0.8	<0.03	0.62	<0.1	12.5	n.d.	-66.0	-10.1	0.340	-9.0	-3.49	-6.18
24	R4	0.04	1.4	3.4	<0.05	0.22	<0.2	43.3	n.d.	-68.7	-10.0	0.758	-9.2	-1.38	-1.94
25	R5	0.04	0.8	0.7	<0.05	<0.1	<0.2	29.3	n.d.	-69.9	-10.0	0.768	-8.7	-2.75	-4.69
26	R6	<0.03	0.5	0.6	<0.05	<0.1	<0.2	16.2	n.d.	-66.1	-9.7	0.364	-6.1	-2.97	-5.19

n.a = not analyzed; n.d = not detected; TDIC = Total dissolved inorganic carbon; SI = Saturation index.

† Geochemical and isotope data from Wrage et al. (2017)

Table 2.1: (continued)

#	ID	CFC-12 [pmol/L]	CFC-11 [pmol/L]	CFC-113 [pmol/L]	SF_6 [fmol/L]
1	AV	0.12 ± 0.05	0.19 ± 0.05	0.02 ± 0.05	0.5 ± 0.1
2	PE	0.18 ± 0.05	0.24 ± 0.05	0.03 ± 0.05	0.3 ± 0.1
3	NI	n.a	n.a	n.a	n.a
4	NI	2.5 ± 0.20	4.3 ± 0.60	0.42 ± 0.05	3.0 ± 0.3
5	MA	0.11 ± 0.05	0.19 ± 0.05	0.02 ± 0.05	0.3 ± 0.1
6	MA	n.a	n.a	n.a	n.a
7	JM	n.a	n.a	n.a	n.a
8	CU	2.8 ± 0.20	5.3 ± 0.60	0.49 ± 0.05	3.4 ± 0.4
9	VL	n.a	n.a	n.a	n.a
10	VL	1.7 ± 0.10	2.4 ± 0.30	0.25 ± 0.05	2.6 ± 0.3
11	MZ	0.33 ± 0.05	0.48 ± 0.05	0.05 ± 0.05	0.5 ± 0.1
12	MZ	0.05 ± 0.05	0.08 ± 0.05	0.01 ± 0.05	0.3 ± 0.1
13	AM	2.2 ± 0.20	1.6 ± 0.20	0.19 ± 0.05	2.2 ± 0.3
14	ML	2.4 ± 0.20	4.1 ± 0.50	0.35 ± 0.05	1.4 ± 0.2
15	CG	0.15 ± 0.05	0.09 ± 0.05	<0.01	0.1 ± 0.1
16	CG	0.38 ± 0.05	0.41 ± 0.05	0.04 ± 0.05	0.3 ± 0.1
17	PO	0.55 ± 0.05	0.90 ± 0.10	0.07 ± 0.05	0.6 ± 0.1
18	CB	2.2 ± 0.20	2.8 ± 0.30	0.28 ± 0.05	1.5 ± 0.2
19	BT	n.a	n.a	n.a	n.a
20	VA	0.71 ± 0.05	0.9 ± 0.10	0.09 ± 0.05	0.5 ± 0.1

n.a = not analyzed.

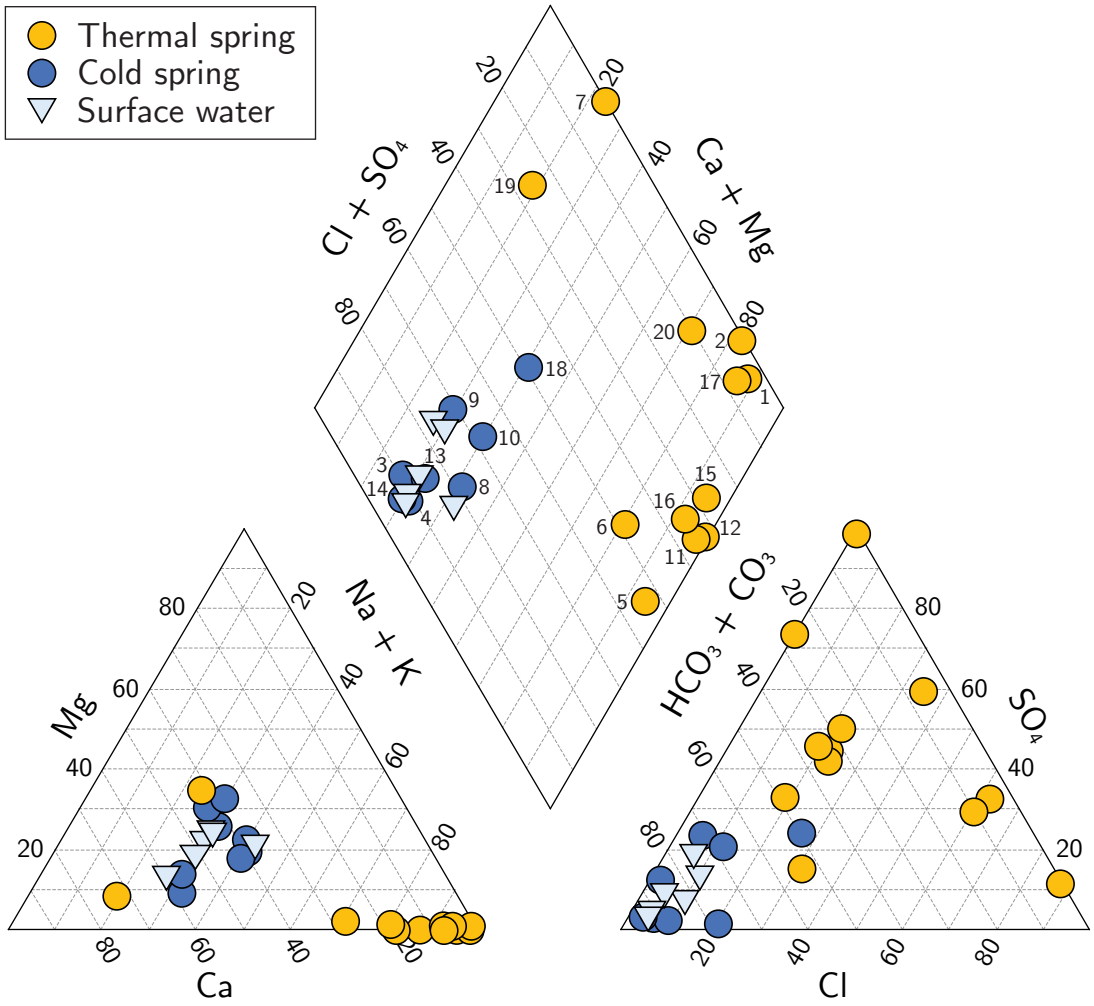

Figure 2.2: Piper diagram comparing the ionic composition of cold groundwater, surface water, and hot spring samples. The lower left and right ternary plots show major cation and anion concentrations, respectively, which are then projected into the diamond. Concentrations are in Eq/L.

isotope analyses from this study, we compiled all available isotopic data in precipitation in the Araucanía region of Chile. The dataset includes values from the International Atomic Energy Agency's Global Network of Isotopes in Precipitation (GNIP) (IAEA/WMO, 2018) and reports from Chile's National Water Board (Dirección General de Aguas, 2016). A total of 47 samples from 21 locations between 38–39.5°S were compiled (Appendix A, Supplementary Material A.1). We applied a linear-regression analysis to establish the local meteoric water line. To verify quality of the dataset and rule out the effects of secondary processes—such as partial evaporation during sampling or site-specific environmental conditions—deuterium excess ($d \equiv \delta^2\mathrm{H} - 8 \cdot \delta^{18}\mathrm{O}$, defined by Dansgaard (1964)) was calculated for each data point. Distribution of d–excess values was tested for normality. No statistically significant deviation from a normal distribution was observed (Skew = 0.06; Kurtosis = 1.08; Shapiro-Wilk test W = 0.975 with p-value = 0.55). Outliers were discarded via Chauvenet's Criterion (Taylor, 1997; Benjamin et al., 2005) and the best-fit line was calculated via the least squares method. A total of 2 samples were removed from the database (4.3% of the data set). The resulting local meteoric water line and its corresponding equation are shown in Figure 2.3.

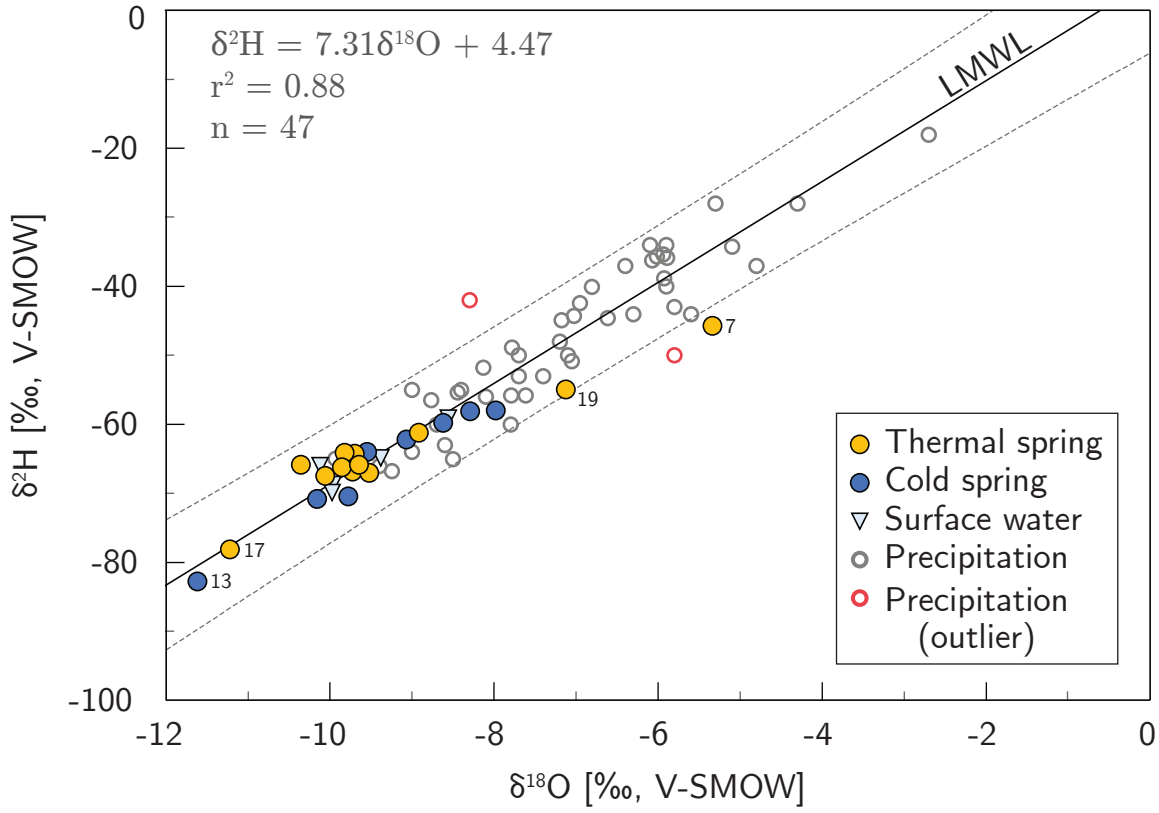

Figure 2.3: δ^{18}O vs. δ^{2}H plot. Gray circles represent the isotopic composition of precipitation samples from the SVZ between 38 and 39°S. Red circles are outliers discarded from the database. Black line represents the local meteoric water line (LMWL), calculated by linear regression via the least squares method (corresponding equation in the upper left). Dashed lines represent the 2σ prediction interval for samples (95% probability) of the linear regression. Excluding JM(7) and BT(19), samples fall within the 2σ-prediction interval of the meteoric linear regression, indicating with high probability that small deviations from the LMWL are within the natural spread of source precipitation isotope composition, and the δ^{18}O and δ^{2}H values of these waters likely did not suffer major changes during subsurface circulation.

$\delta^{13}C_{TDIC}$

The inorganic carbon isotope composition of samples is presented in Table 2.2. Thermal and cold groundwater isotope compositions overlap, with cold groundwaters being generally more depleted in the heavier isotope (thermal springs: -17.4 to -10.1‰, average -14.1‰, cold groundwater: -20.3 to -5.1‰, average -16‰). One cold groundwater sample (VL(9)) had an anomalously high (-5.1‰) isotopic composition compared to other samples, due to mixing with river water near discharge point. All surface water samples (-9 to -5.1‰) have compositions near atmospheric equilibrium due to continuous exchange with the atmosphere. JM(7) and BT(19) thermal waters could not be sampled for $\delta^{13}C_{TDIC}$, although the $\delta^{13}C_{CO_2}$ values of the associated fumaroles in these geothermal areas are reported in Tardani et al. (2016) as -9.75 and -8.79‰, respectively.

2.4.3 Dissolved anthropogenic tracer concentration

Dissolved anthropogenic tracer concentrations of groundwater samples are presented in Table 2.1. Low but detectable concentrations of all tracers were measured in geothermal springs (CFC-12: 0.05–0.71 pmol L^{-1}; CFC-11: 0.08–0.9 pmol L^{-1}; CFC-113: 0.01–0.09 pmol L^{-1}; SF_6: 0.1–0.5 fmol L^{-1}), with only one sample (CG(15)) being below detection limit for CFC-113. The two high-temperature sulfate springs, JM(7) and BT(19), were not considered for tracer analysis due to the fact that boiling processes, which could affect dissolved tracer concentrations, could not be discarded. In contrast to thermal waters, cold groundwater samples have significantly higher concentrations of all tracers (CFC-12: 1.7–2.8 pmol L^{-1}; CFC-11: 1.6–5.3 pmol L^{-1}; CFC-113: 0.19–0.49 pmol L^{-1}; SF_6: 1.4–3.4 fmol L^{-1}) pointing towards a much more recent infiltration.

2.5 Discussion

The chemical, isotopic, and anthropogenic tracer data presented above reveals differences in water samples based on their temperature, despite proximity of outflow points. In the following section, we examine these differences and discuss possible subsurface processes (e.g. fractionation, mixing, fluid-rock interaction) as well as the implications of these data for fluid source and circulation in a complex fractured hydrogeological setting.

2.5.1 Hydrothermal system recharge

Excluding JM(7) and BT(19) samples, thermal waters display no significant deviation from the LMWL (Fig. 2.3), despite a shift commonly being observed in geothermal systems around the world, due to the progressive equilibration of thermal fluid with host-rocks (Craig, 1963; Giggenbach, 1992). This may be due to insufficient temperatures for isotopic exchange, or indicative of a system with high permeability leading to increased water/rock ratios (Druschel and Rosenberg, 2001). Additionally, small changes in isotopic signature having occurred at depth can be partially masked by mixing with meteoric fluids during ascent. The relative enrichment in the heavier isotopes of oxygen and hydrogen in JM(7) and BT(19) indicate either boiling at depth, or mixing with magmatically-derived, "andesitic" waters (e.g. Giggenbach, 1997; Wrage et al., 2017).

The predominantly meteoric origin of thermal waters (Fig. 2.3) is consistent with previous studies in the SVZ (e.g. Muñoz et al., 2011; Sánchez et al., 2013; Wrage et al., 2017; Negri et al., 2018). However, the aforementioned studies do not address the relation of thermal fluid isotopic composition with that of local precipitation, or the implications of the orographic effect on system recharge. Due to the scarcity of data in southern Chile on the isotope composition of rainfall throughout the year and at high altitude stations, we applied a mathematical model to determine the vertical variation of oxygen isotope ratios in precipitation ($\delta^{18}O_P$). Moisture in the western slopes of the Andes at ~38°S is principally derived from evaporation at the Pacific Ocean and carried over the continent by prevailing westerly

winds (Garreaud, 2009). As it migrates inland, the moist parcel of air is forced aloft as it encounters higher elevations. This lift in air-mass is known as the orographic effect, and isotope fractionation in this model is driven primarily by the accompanying decrease in temperature (Rozanski et al., 1993). The progressive depletion of rainwater in heavier isotopes with increasing altitude is modelled to first order by a Rayleigh-type distillation process, in which condensate is continuously removed from air-mass vapor during its ascent (Dansgaard, 1964; Stöwhas and Moyano, 1993; Rozanski et al., 1993; Rowley et al., 2001; Rowley, 2007). The Rayleigh model is coupled with a one-dimensional simulation of the ascent, cooling and subsequent condensation of atmospheric moisture from a low elevation source. A full description of equations applied in the model is provided in Appendix B. The boundary conditions required to compute the vertical variation of $\delta^{18}O_P$ are starting temperature, relative humidity and isotope composition of the vapor ($\delta^{18}O_V$) prior to saturation. As a starting point we chose the Temuco weather station (114 m a.s.l., Fig. 2.1a), which is located to the west of the study area—the direction from which moisture is derived at sea—and is the point in the Araucanía region were the most complete meteorological data is available. The starting value of $\delta^{18}O_V$ was chosen to yield precipitation compatible with local GNIP data at Temuco. Figure 2.4 shows the $\delta^{18}O$ values of water samples versus discharge elevation, compared to the isotope composition of precipitation based on our Rayleigh-fractionation model. Assuming isotopic composition was not altered during subsurface circulation (Fig. 2.3), the $\delta^{18}O$ values of samples can be extrapolated to the curves to determine mean recharge elevation (e.g. James et al., 2000; Kelly and Glenn, 2015).

Three cold groundwater samples (NI(3), NI(4), and CU(8)) plot above the mean annual precipitation curve (Fig. 2.4). This may initially seem counterintuitive, as it would imply that average annual recharge for these samples occurs below discharge point. However, samples in these two areas also had the highest anthropogenic tracer concentrations (Table 2.1), indicating modern day recharge and, consequently, a larger seasonal component. Thus, recharge altitude for these samples was calculated based on the summer curve. Three hot spring samples (MA(5), MA(6), VA(20)), also plot above the annual curve (Fig. 2.4). A seasonal component in thermal springs is unlikely, as these are predominantly old (pre-1940) waters, and seasonal variations tend to be "smoothed-out" in old, well-mixed groundwater systems. Assuming no boiling at depth or evaporation modified their isotopic signature (Fig. 2.3), we observe that these samples are all high-altitude springs discharging on the flanks of the Tolhuaca and Sierra Nevada volcanoes, respectively, and correspond to high-temperature geothermal systems with associated fumarole activity (Melosh et al., 2010, 2012). These springs are likely located near the upflow zones of their respective systems, where thermal buoyancy of water causes upward flow along vertical fracture zones. Meteoric recharge for these convection-dominated volcanic systems likely occurs along fault zones and permeable sediments/soils at the base of volcanoes, is heated at depth, and rises along vertical fractures in volcanic rocks (Moeck, 2014).

The estimated recharge altitude of each sample is presented in Table 2.2. Based on our model, geothermal system recharge in the south-west basin formed by the volcanic arc (areas MA, MZ, CG, and VA, see Fig. 2.1c) occurs at average elevations near ∼1000 and up to ∼1200 m a.s.l. These altitudes correspond roughly to precipitation occurring at the margins of valleys and the lower flanks of mountain chains (Fig. 2.1c), where the bulk of precipitation is expected to occur due to orographic uplift as moist air is forced upwards along steep

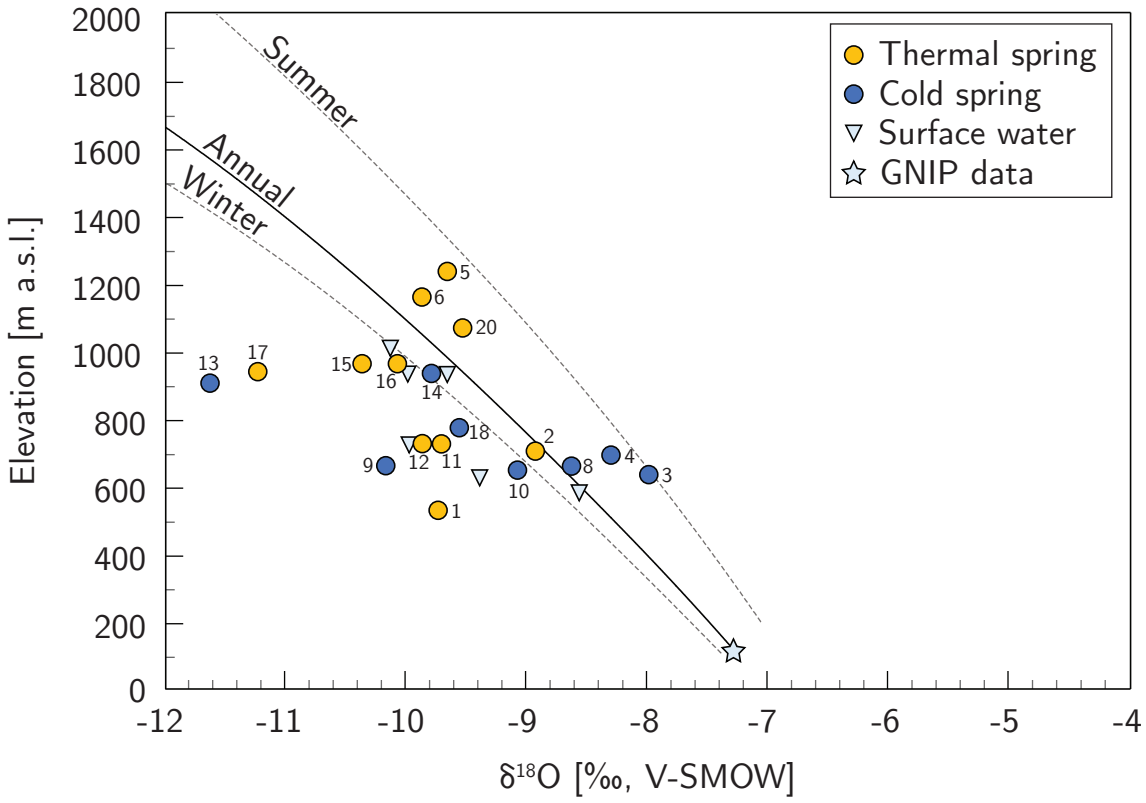

Figure 2.4: δ^{18}O vs. sampling elevation of waters from this study. Curves represent the isotopic composition of precipitation as a function of ground elevation using a Rayleigh fractionation model, based on average annual, winter (Dec–Feb), and summer (Jun–Aug) climate conditions. Blue star represents the volume-weighted GNIP data of Temuco weather station, taken as border conditions for the model.

gradients. Favorably-oriented faults (LOFS, Fig. 2.1b) and fracture zones present across these flanks and valleys constitute high vertical permeability pathways that allow recharge to reach deep levels of this thermal area (Tardani et al., 2016; Pérez-Flores et al., 2017b).

AM(13) and PO(17) samples are depleted in δ^{18}O and δ^{2}H values with regard to other samples from this study (Fig 2.3). These samples belong to a different drainage basin, east of the volcanic arc formed by the LTVC and Sierra Nevada, and are likely hydraulically disconnected from the rest of the system. The isotopic depletion of these samples, located east of a high-altitude, steep-slope terrain (Fig 2.1c) is consistent with our model assumption that topography is the dominant factor modulating the isotope ratio of precipitation (and therefore, of system recharge), as the orographic uplift of air would lead to enhanced precipitation on the windward side (west) of the mountain range, leaving relatively depleted isotope ratios on the leeward side (east). Stern and Blisniuk (2002) observed this "isotopic rain-shadow" effect farther south in the Patagonian Andes was able to generate δ^{18}O values up to $\sim 4‰$ lower on the east side compared to the west. The Coyuco geothermal area (not included in this study), located 50 km directly east of the LTVC, at approximately 1600 m a.s.l., reports an even more depleted meteoric signature of $\delta^{18}\text{O} = -87.6‰$ and $\delta^{2}\text{H} = -12.4‰$ (Wrage et al., 2017), supporting this hypothesis.

Table 2.2: Summary characteristics of hot and cold springs. Samples are listed by geographic location from north to south.

#	ID	Sampling date	Location* Easting	Location* Northing	Outflow Elevation m a.s.l.	Outflow Temp. °C	Recharge Elevation m a.s.l.	Recharge Temp. °C	Equivalent atmospheric mixing ratio CFC-12 [pptv]	CFC-11 [pptv]	CFC-113 [pptv]	SF_6 [pptv]
Hot springs												
01	AV	2017/04/15	277623	5792326	535	67.8	1011	7.0	21.49	8.68	2.91	1.27
02	PE	2017/04/11	263072	5782280	710	36.1	737	8.8	34.20	11.75	4.72	0.80
05	MA	2017/04/13	261523	5764434	1241	84.6	987	7.2	19.81	8.73	2.93	0.76
06	MA	2018/05/07	261451	5765257	1165	30.8	1055	6.7	-	-	-	-
07	JM	2014/01/14	266696	5758625	2105	92.0	-	-	-	-	-	-
11	MZ	2017/04/10	263738	5739080	732	45.4	1003	7.1	59.35	22.02	7.31	1.27
12	MZ	2017/04/10	263715	5739024	734	48.2	1055	6.7	8.86	3.61	1.43	0.76
15	CG	2017/04/10	274480	5736573	968	40.5	1212	5.7	26.68	3.90	n.d.	0.25
16	CG	2017/04/10	274480	5736573	968	40.2	1120	6.3	66.43	18.19	5.63	0.75
17	PO	2018/05/03	289182	5732951	945	32.7	1465	4.1	88.72	36.32	8.85	1.41
19	BT	2013/03/27	272137	5727180	1362	95.7	-	-	-	-	-	-
20	VA	2017/04/14	271097	5726641	1074	63.2	944	7.4	129.06	41.82	13.34	1.28
Cold Springs												
03	NI	2018/05/04	248525	5773548	643	11.8	656	9.3	-	-	-	-
04	NI	2018/05/04	247743	5773517	698	10.4	794	8.4	469.35	207.57	65.03	7.89
08	CU	2018/05/02	245946	5747882	665	11.0	934	7.5	510.09	246.88	72.86	8.74
09	VL	2018/05/05	256658	5739110	667	9.7	1150	6.1	-	-	-	-
10	VL	2018/05/05	255768	5739368	654	13.2	790	8.4	319.43	115.97	38.75	6.84
13	AM	2017/04/09	293689	5738927	911	11.3	1572	3.4	345.77	62.62	23.20	5.07
14	ML	2018/05/03	274910	5738246	940	8.4	1029	6.9	428.18	186.32	50.60	3.54
18	CB	2017/04/12	266164	5729992	779	12.0	953	7.4	399.13	129.79	41.40	3.85

n.d. = not detected. Tracer concentration below detection limit.

*WGS84/UTM zone 19S

Table 2.2: (continued)

#	ID	Piston Flow Model Recharge Year				Binary Mixing Model Young water fraction in mixture					Binary Mixing Model Age of young component				
		CFC-12	CFC-11	CFC-113	SF_6	$SF_6/C12$	$SF_6/C11$	$SF_6/C113$	$C11/C113$	$C12/C113$	$SF_6/C12$	$SF_6/C11$	$SF_6/C113$	$C11/C113$	$C12/C113$
Hot Springs															
01	AV	1958	1960	1970	1984	n.p.	n.p.	n.p.	0.04	0.05	n.p.	n.p.	n.p.	2016	1990
02	PE	1961	1962	1972	1980	0.08	n.p.	n.p.	0.06	0.07	2016	n.p.	n.p.	2016	1990
05	MA	1957	1960	1970	1980	n.p.	n.p.	n.p.	0.04	0.04	n.p.	n.p.	n.p.	2016	1992
06	MA	-	-	-	-	-	-	-	-	-	-	-	-	-	-
07	JM	-	-	-	-	-	-	-	-	-	-	-	-	-	-
11	MZ	1965	1965	1974	1984	0.13	n.p.	n.p.	0.10	0.14	2016	n.p.	n.p.	2016	1989
12	MZ	1952	1956	1967	1980	n.p.	n.p.	n.p.	0.02	0.02	n.p.	n.p.	n.p.	2016	2016
15	CG	1959	1956	n.d.	1972	0.04	0.03	n.d.	n.d.	n.d.	2004	2016	n.d.	n.d.	n.d.
16	CG	1966	1964	1973	1980	0.11	0.09	0.08	0.07	0.19	2008	2016	2016	1995	1984
17	PO	1968	1968	1976	1985	0.17	0.17	n.p.	0.15	0.23	2015	2016	n.p.	1989	1986
19	BT	-	-	-	-	-	-	-	-	-	-	-	-	-	-
20	VA	1971	1969	1978	1984	0.22	0.18	0.18	0.18	0.33	2005	2012	2012	2016	1987
Cold Springs															
03	NI	-	-	-	-	-	-	-	-	-	-	-	-	-	-
04	NI	1990	1986	1990	2014	0.92	0.95	0.93	0.79	1.00	2016	2016	2016	1996	1990
08	CU	2016†	2008†	2014†	2016	1.00	1.00	1.00	0.97	1.00	2016	2015	2016	1992	1991
09	VL	-	-	-	-	-	-	-	-	-	-	-	-	-	-
10	VL	1982	1976	1986	2010	n.p.	n.p.	n.p.	n.p.	0.76	n.p.	n.p.	n.p.	n.p.	1988
13	AM	1984	1972	1982	2003	0.67	n.p.	n.p.	n.p.	n.p.	2013	n.p.	n.p.	n.p.	n.p.
14	ML	1988	1984	1988	1996	0.77	0.74	0.65	0.74	1.00	2001	2002	2005	1991	1988
18	CB	1987	1978	1987	1998	0.68	0.55	0.56	0.57	1.00	2004	2011	2011	2016	1987

n.d = not detected. Tracer concentration below detection limit.

n.p = not possible. Tracer ratios are incongruent with historic atmospheric concentrations.

† Dual ages are derived. Only the younger of two possible ages is shown.

2.5.2 Sources of inorganic carbon

In Figure 2.5, the total dissolved inorganic carbon (TDIC) and $\delta^{13}C_{TDIC}$ values of samples from this study are compared. The blue star represents the calculated composition of average rainwater from the study area (pH = 5.6, Temp. = 10°C) in equilibrium with atmospheric CO_2 ($PCO_2 = 10^{-4}$ atm, $\delta^{13}C = -7‰$) based on the isotope equilibrium fractionation factors of Zhang et al. (1995). Gray lines are theoretical curves representing the evolution of infiltrating rainwater during the addition of soil CO_2. Partial pressure of CO_2 (PCO_2) in soil is significantly higher than PCO_2 of the atmosphere, and thus CO_2 derived from the oxidation of organic matter and root respiration will readily dissolve in groundwater as it percolates downwards (e.g. Cerling, 1984; Appelo and Postma, 2005). The selected $\delta^{13}C_{TDIC}$ values, ranging from −15 to −27‰, are reported by several authors as indicative of soil CO_2 derived from biogenic sources in non-arid, temperate climates (Rightmire and Hanshaw, 1973; Deines et al., 1974; Cerling, 1984; Rose and Davisson, 1996; Chiodini et al., 2000). For the magmatic CO_2 input, we assumed ranges of −7.5 to −10‰, based on reported data from Tardani et al. (2016) of deeply-derived fumarole gas in the SVZ. These magmatic values are interpreted as having a MORB-like signature of CO_2 ($\delta^{13}C = -6.5 \pm 2.2$, Sano and Marty (1995)) with small degrees of crustal contamination (−28 to +6‰, Oehlert and Swart (2014)).

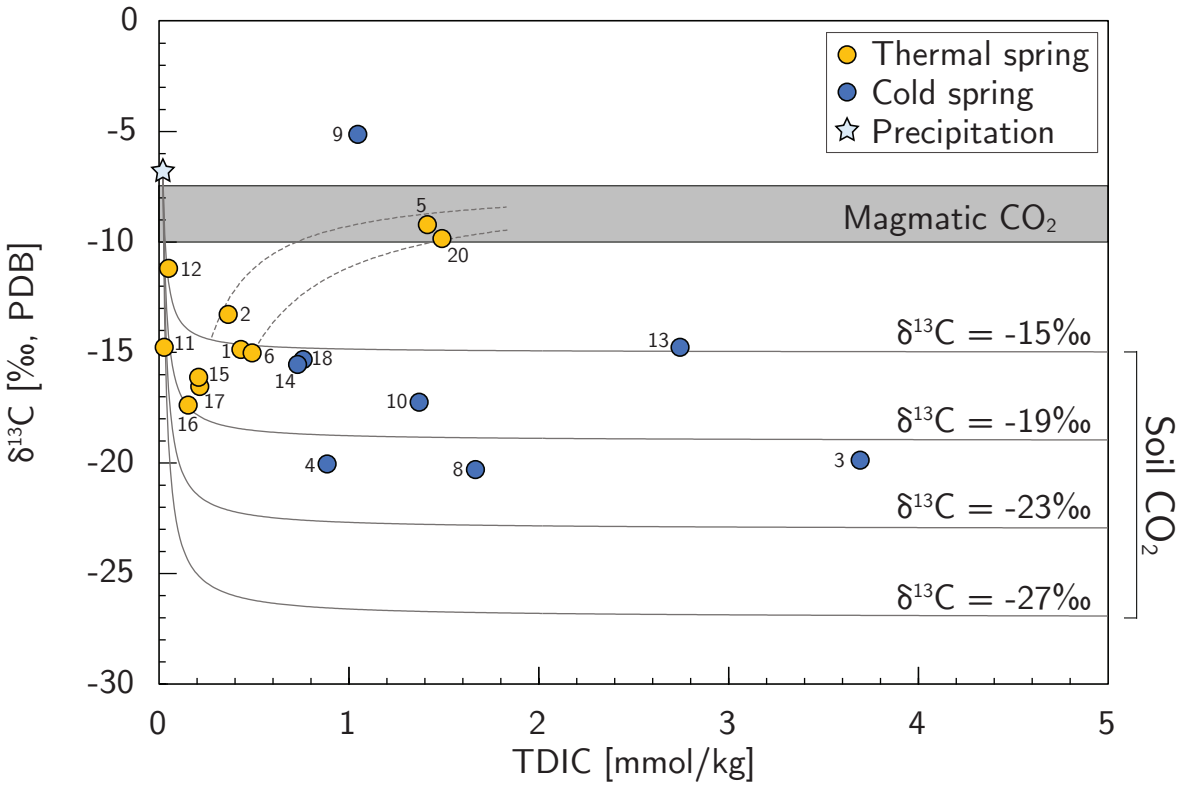

Figure 2.5: Total dissolved inorganic carbon concentration versus $\delta^{13}C$ of cold groundwater and thermal springs. Blue star represents precipitation in equilibrium with atmospheric air. Curves represent the evolution of fluid composition during the addition of soil CO_2 with different $\delta^{13}C$ values. Magmatic CO_2 field is shown (based on Tardani et al. (2016)). Dashed curves represent possible evolution paths of thermal water during the addition of magmatic CO_2.

Results are consistent with the bulk of dissolved inorganic C being derived from the

addition of soil CO_2 to an atmospheric source. Geothermal samples MA(5) and VA(20) are relatively enriched in C with regard to other thermal springs, and have more positive $\delta^{13}C$ values, corresponding to a magmatic signature. Dashed lines in Figure 2.5 represent possible evolution paths for geothermal waters during the addition of magmatic CO_2. The addition of magmatically-derived CO_2 in these geothermal areas is consistent with their proximity to volcanic centers (LTVC and Sierra Nevada, respectively, see Fig 2.1b) and active fumarole fields.

The relatively low TDIC contents of thermal waters and the more positive $\delta^{13}C$ values when compared to cold groundwater (Fig. 2.5) are suggestive of C loss by CO_2 degassing and subsequent calcite precipitation. These processes commonly affect hydrothermal fluids as they ascend to the surface, either due to loss of temperature and depressurization or by mixing with shallow groundwater. Figure 2.6 illustrates the saturation indices of calcite and dolomite, the two most commonly occurring carbonate minerals, of samples as a function of pH. Cold groundwater samples tend to be severely subsaturated for both minerals (SI < -1, with the exception of AM(13) sample), while thermal waters approach calcite saturation (SI ~ 0), suggesting that precipitation of this mineral likely occurred during ascent. To explore the effects of degassing and calcite precipitation on the $\delta^{13}C$ values of fluid, we model C-isotope distribution in the $CaCO_3$–CO_2(g)–H_2O system, assuming CO_2(g) and calcite are continuously removed from the solution (in order to simulate the open system conditions of the ascending fluid), using PHREEQC geochemical modeling program and the iso.dat database (Parkhurst and Appelo, 2013). In this model, we consider a theoretical fluid of meteoric origin, representative of our geothermal system recharge, having initially percolated through soil prior to heating at depth and with no magmatic CO_2 input. The composition of TDIC is $1.7\,\mathrm{mmol\,kg^{-1}}$ and $\delta^{13}C = -17.6‰$ (average composition of cold groundwater samples from this study, not considering contaminated sample VL(9)), and is saturated in Ca with respect to $CaCO_3$. pH of the initial fluid is adjusted to maintain charge balance. In each step, a fixed volume of CO_2(g) (0.1 L) is removed from the fluid and calcite is allowed to precipitate. The distribution of ^{13}C is then calculated among the calcite, gas phase, and solute species of C (CO_2(aq), HCO_3^-, CO_3^{2-}). Figure 2.7 shows the composition of the fluid as it approaches equilibrium with surface conditions (PCO_2(g) $= 10^{-4}$ atm)at different temperatures relevant to thermal systems in the SVZ. The PHREEQC code developed for this model is provided in Appendix A, Supplementary Material A.4. Results from our modeling show that degassing and calcite precipitation at temperatures below ~200°C, likely occurring by depressurization of the ascending thermal fluid or mixing with shallow groundwater, can account for the enriched $\delta^{13}C$ signature of some thermal springs in the SVZ. This model is consistent with observations from Pérez-Flores et al. (2016), which reported mineral assemblages including calcite, occurring within fault-fracture networks, indicating crystallization temperatures between 110–170°C. In the following section, we present anthropogenic tracer data to explore the groundwater mixing hypothesis in further detail.

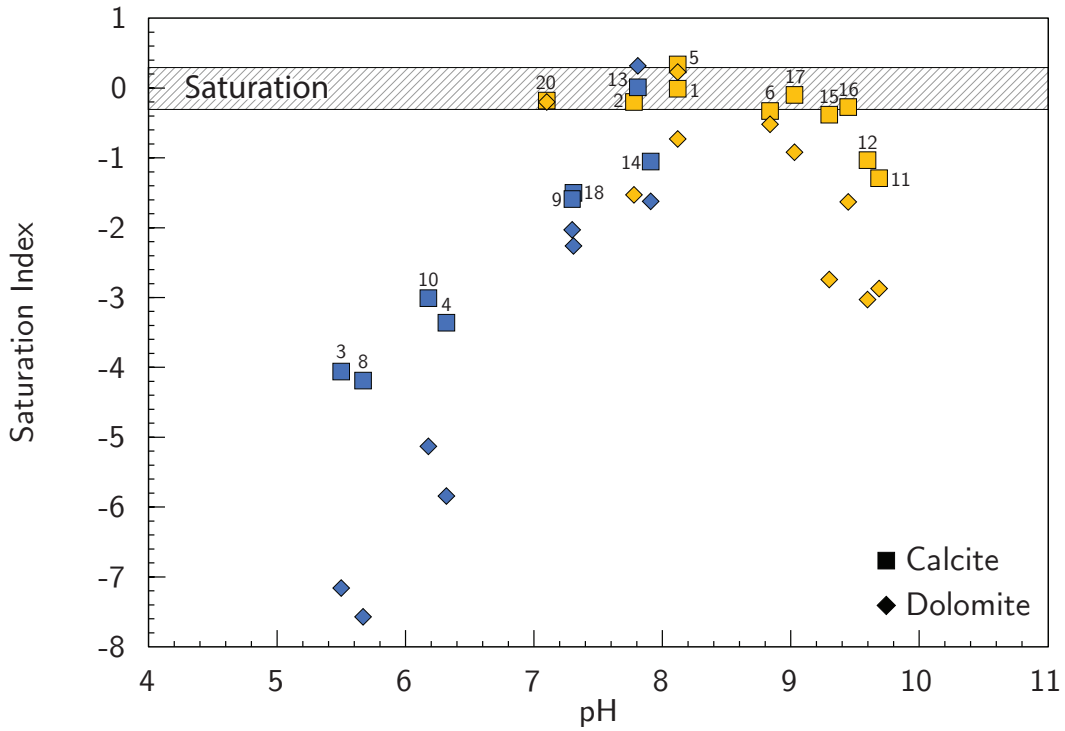

Figure 2.6: Saturation indices of calcite and dolomite in cold groundwater (blue) and hot spring samples (yellow) as a function of pH. Field with diagonal lines represents mineral saturation.

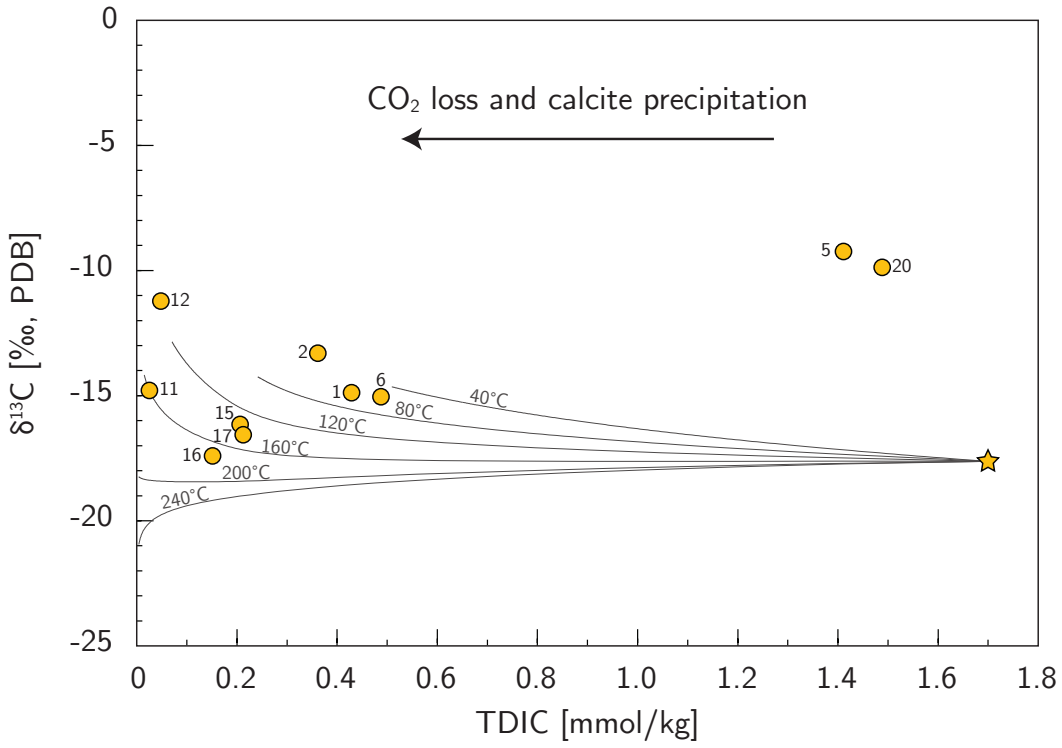

Figure 2.7: Effects of CO_2 degassing and calcite precipitation on a fluid, modeled at different temperatures relevant to geothermal systems in the SVZ. Star denotes the initial composition of the fluid, calculated as the average composition of cold groundwater samples from this study, and considered representative of hydrothermal system recharge. Samples MA(5) and VA(20) show an aditional source of magmatic C.

2.5.3 Groundwater residence times and mixing of fluids of different ages

Using the methodologies described in Plummer et al. (2006a) and Busenberg and Plummer (2006), the atmospheric concentration of CFCs and SF_6 during recharge can be reconstructed as a function of concentration in the water sample, and thus assigned an age. Briefly, dating with these low concentration gases is based on Henry's Law solubility, in which the concentration of a particular tracer C_{i}, dissolved in water in equilibrium with air, is given by:

$$C_{\mathrm{i}} = K_{H_{\mathrm{i}}} X_{\mathrm{i}} (P - p_{\mathrm{H_2O}}) \tag{2.1}$$

where $K_{H_{\mathrm{i}}}$ is the Henry's Law constant for the ith tracer, x_{i} is the dry air mole fraction of C_{i}, P is the total atmospheric pressure, and $p\mathrm{H_2O}$ is the water vapor pressure. P is a function of mean recharge altitude (Table 2.2), and $K_{H_{\mathrm{i}}}$ and $p_{\mathrm{H_2O}}$ are well-established functions of temperature (Weiss and Price, 1980; Warner and Weiss, 1985; Bu and Warner, 1995; Bullister et al., 2002) during recharge. Recharge temperature was approximated as mean annual temperature based on measurements from a local weather monitoring station (10 °C mean annual air temperature at 550 m a.s.l. at Curacautín station, see Fig. 2.1c) and corrected for altitude at an International Standard Atmosphere lapse rate of 0.0065 °C per meter of elevation (ISO, 1975). Once calculated, the dry air mole fraction of a particular tracer is replaced by the dry air mixing ratio, volume per volume (assuming ideal gas behavior) and compared to the corresponding historical atmospheric mixing ratio in the Southern Hemisphere to determine recharge year (Table 2.2).

Derived apparent recharge year of groundwater samples based on direct age determination for each tracer (simple matching of sample and atmospheric concentrations) is presented in Figure 2.8a. The Southern Hemisphere atmospheric concentration curves used to calculate recharge year are presented in Figure 2.8b. In accordance with their respective tracer concentrations, samples that classified as thermal are characterized by substantially older apparent ages than samples classified as cold. For one cold water sample (CU(8)), dual ages are derived from CFC-11, 12 and 113 concentrations. Derivation of dual ages from CFC dating is possible due to the decreasing atmospheric concentration of these tracers in recent decades. For geothermal water samples, CFC-11 and CFC-12 provide the most similar ages, with CFC-113 giving consistently younger ages by approximately 10 years, and SF_6 biased even younger, by 15 to 20 years (Fig. 2.8a). On the other hand, CFC-12 and CFC-113 give the best match in ages for cold springs, with CFC-11 providing older ages (5 to 12 years) and SF_6 being much younger (up to 28 years for one sample). These apparent discrepancies can occur when either: (a) mixing of fluids of different ages occurs (Plummer et al., 2006b) or (b) secondary processes are affecting anthropogenic tracer composition, such as bacterial degradation or site-specific contamination (Cook et al., 2006). Both alternatives are discussed in the following sections.

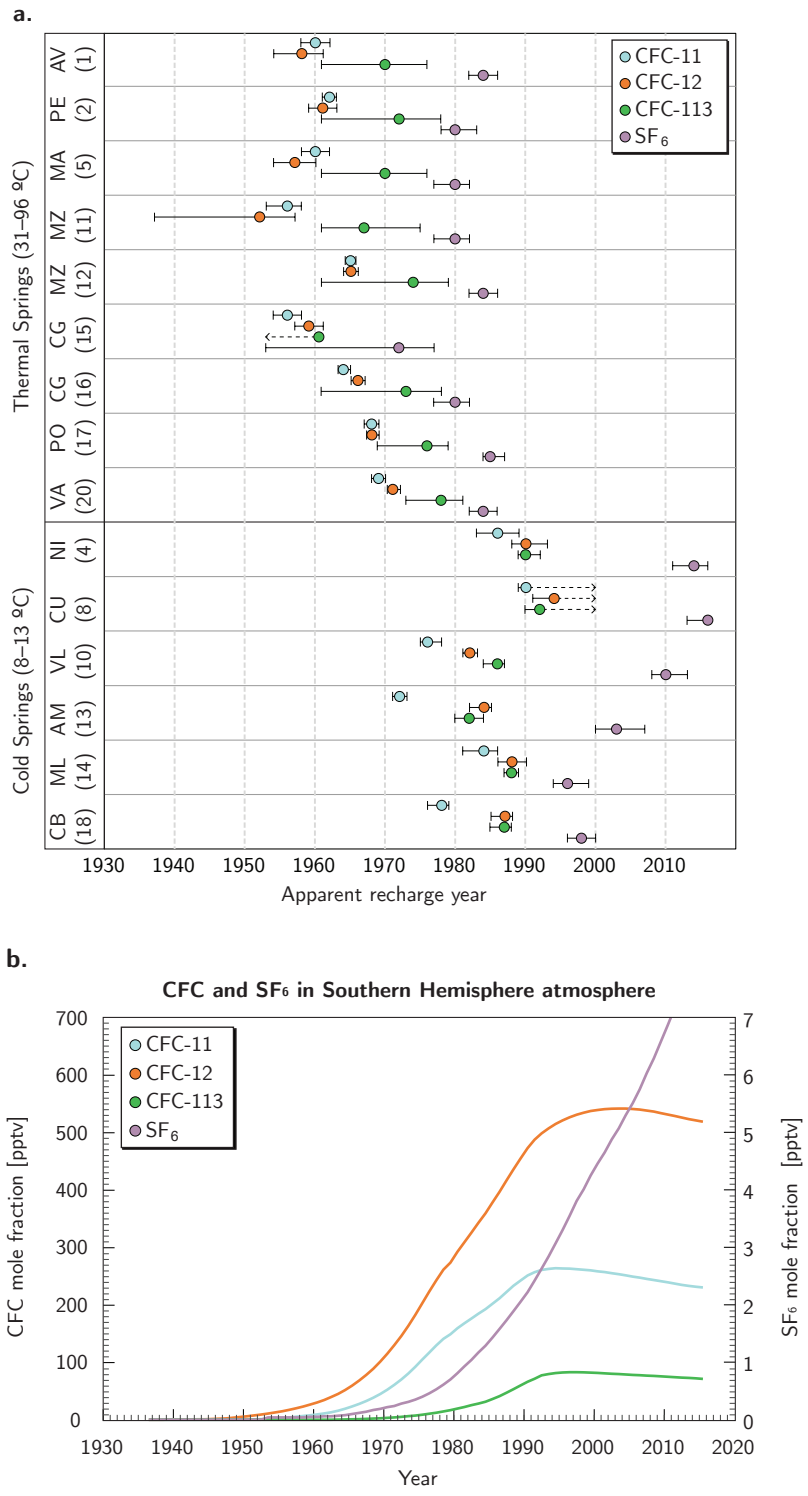

Figure 2.8: **(a)** Derived apparent recharge year of thermal and cold groundwater samples, based on direct age determination for each tracer (CFC-11, CFC-12, CFC-113, and SF_6). Whiskers represent analytical error. CFC-113 concentrations of CG(15) sample are below detection limit. Dual ages are derived for CU sample for all CFCs. **(b)** Southern Hemisphere atmospheric concentrations of CFC-11, CFC-12, CFC-113, and SF_6 used in age determination of samples. Data from NOAA (available at ftp://ftp.cmdl.noaa.gov/hats/).

Subsurface mixing in a geothermal context

Subsurface flow through different media such as permeable strata or fractured rocks will induce different mixing patterns in water discharging from wells or springs. Fluids ascending through focused, permeable pathways will be relatively unmixed, while springs discharging from diffuse-flow systems will be more affected by mixing (Plummer et al., 2006b; Held et al., 2018). Subsurface groundwater mixing was modeled using a piston flow, binary mixing, and exponential mixing approach (Małoszewski and Zuber, 1982), then compared to the observed tracer concentrations of thermal and cold springs in the study area. The results of this comparison are presented in Figure 2.9.

Piston flow describes the expected concentrations (C) of a tracer dissolved in groundwater discharging from a single, laminar flow path with no mixing. Mathematically, this is expressed as

$$C(t_{obs}) = C_{atm}(t_{obs} - t')\mathrm{e}^{-\lambda} \tag{2.2}$$

where t_{obs} is the time of observation, t' is the age of the water parcel, and C_{atm} is the atmospheric input function for the respective tracer (Fig. 2.8b). An exponential decay factor, λ, accounts for possible bacterial degradation of the tracer. When $\lambda = 0$, the piston flow model is equivalent to simple matching of fluid and atmospheric concentrations. Binary mixing describes a simple, two end-member mixture of differently weighted water bodies with different tracer concentrations (C_1, C_2), given by:

$$C(t_{obs}) = C_1 X + C_2(1 - X) \tag{2.3}$$

where X represents the mixing fraction between both fluids. For readability's sake, we only plot a binary mixing line between old (<1940), tracer-free fluid and a present-day component, although mixing of fluids of any ages is possible. Exponential mixing describes complete mixing of multiple water bodies with an exponential age distribution. Physically, it represents sampling from a homogenous, unconfined aquifer of constant thickness, under the assumption that permeability and porosity decrease exponentially with increasing aquifer depth (Vogel, 1970). If C represents the dissolved tracer concentration of the water parcel, then the exponential model is formulated as:

$$C(t_{obs}) = \int_0^\infty C_{atm}(t_{obs} - t')\mathrm{e}^{-\lambda t'}\frac{1}{\tau}\mathrm{e}^{\frac{-t'}{\tau}}\,\mathrm{d}t' \tag{2.4}$$

where τ is the mean residence time, which is a function of aquifer properties, and all other variables are the same as in the piston flow model. While the above described models may overlap at certain CFC concentration ranges (Fig. 2.9a, 2.9c, 2.9e), the ambiguity between piston flow, binary and exponential mixing at very low concentrations is resolved when plotting SF_6, as the significantly different input function of this tracer generates good separation of plotted curves (Fig. 2.9b, 2.9d).

When observing our data, certain trends become evident. First, geothermal springs show a relatively simple binary mixing pattern, in which tracer-free fluid mixes with a very young groundwater component. This is likely due to older, deeply circulated, ascending hydrothermal fluid that becomes diluted with a small fraction of meteoric water at near-surface levels. As reported on geothermal systems around the world (e.g. Hedenquist, 1991; Gardner et al.,

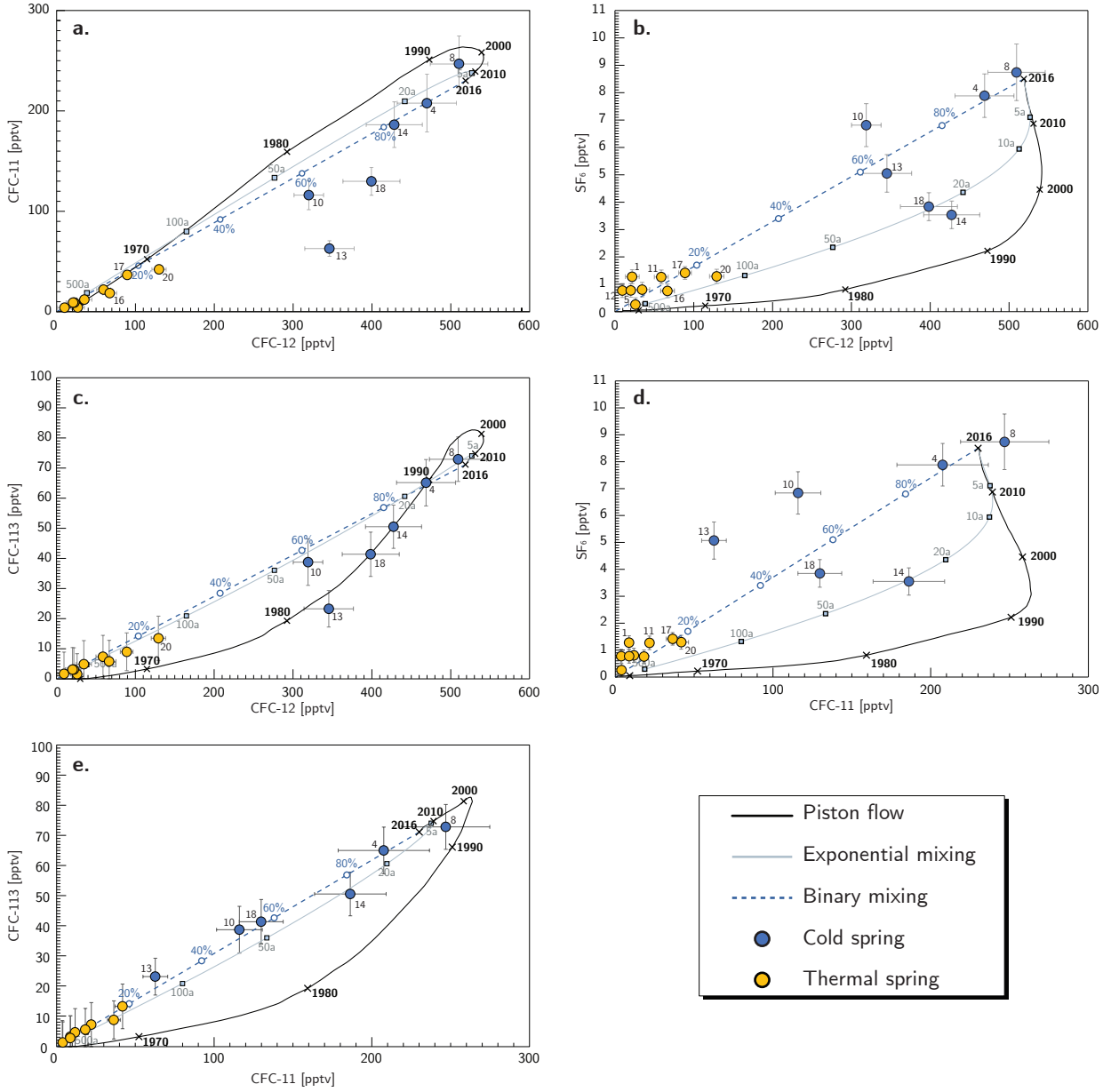

Figure 2.9: Tracer plots comparing concentrations of **(a)** CFC-12 vs. CFC-11, **(b)** CFC-12 vs. SF_6, **(c)** CFC-12 vs. CFC-113, **(d)** CFC-11 vs. SF_6, and **(e)** CFC-11 vs. CFC-113. Black curve represents piston flow model (assuming no bacterial degradation) with crosses marking year of recharge. Gray line represents the exponential mixing model with squares indicating mean transit time. Dashed blue line represents binary mixing between modern and old (tracer-free) groundwater, with circles indicating % of modern groundwater in mix.

2011; Sánchez et al., 2013), mixing with meteoric water in near-surface aquifers is one of the main processes affecting the chemical and isotopic signature of hydrothermal fluids. Secondly, the low mixing fractions of our samples point to a relatively rapid ascent along focused vertical pathways, as opposed to a diffuse ascent, which would have an additional horizontal component and allow for a larger degree of mixing with downwards-percolating, shallow groundwater. When we consider the generally low primary permeability of lithological units in the study area (Pérez-Flores et al., 2017b), the role of fractures facilitating conduit flow from depth to surface becomes apparent. This interpretation is in agreement with data reported by Held et al. (2018)), which similarly observed a binary mixing model best described the age distribution of thermal springs in the Villarrica area, ∼100 km south of the LTVC.

Based on a binary mixing model, we calculate the fraction of modern water and the age of the modern groundwater component using different anthropogenic tracer ratios assuming one tracer-free end-member recharged prior to 1940, and the other recharged after. Results of these calculations are presented in Table 2.2. Thermal springs had an average young water fraction ranging from 2 to 22%. These results are in excellent agreement with data from Tardani et al. (2016), which concluded, based on He isotope and He/Ne ratios from water-dissolved gas samples, that the percentage of air-saturated water of thermal springs in this area fell in a range between 6 and 20%.

On the other hand, cold groundwater samples show a wider distribution, corresponding to more complex mixing patterns, as would be expected from diffuse flow systems. Very young apparent ages in these samples point to shorter flow paths at shallow and near-surface depths. Sample AM(13), VL(10) and CB(18) plot outside the bounding area of atmospheric curves (Fig. 2.9a, 2.9d) indicating some loss of CFC-11 has occurred with respect to other tracers, as well as minor loss of CFC-12 with respect to SF_6 for the AM(13) sample (Fig. 2.9b).

Other processes affecting dissolved anthropogenic tracer concentrations

While there is limited experimental evidence regarding the thermal effects on anthropogenic tracers in groundwater at depth (Darling et al., 2012), CFCs have been successfully applied as dating tools in geothermal systems around the world (Gardner et al., 2011; Edmunds et al., 2014; Rolker et al., 2015; Held et al., 2018). Similarly, SF_6 has been successfully used as an artificially introduced tracer to evaluate bulk water flow in a geothermal reservoir (Upstill-Goddard and Wilkins, 1995). CFCs and SF_6 are chemically inert over a wide range of conditions (Upstill-Goddard and Wilkins, 1995; Cook et al., 2006) and contamination in remote, rural areas away from urban centers is unlikely. Nonetheless, a major concern when dating with CFCs is bacterial degradation, as these tracers have been observed to decay under anaerobic conditions, with CFC-11 being removed much faster than CFC-12 and CFC-113 (Khalil and Rasmussen, 1989; Semprini et al., 1992; Oster et al., 1996; Deipser and Stegmann, 1997). Although partial degradation of all CFCs has been observed in sufficiently reducing environments (e.g. Sebol et al., 2007; Horneman et al., 2008), there have been no reported cases of SF_6 being affected by microbial decay.

The depleted CFC-11 concentrations with respect to other tracers in VL(10), AM(13), and CB(18) cold groundwater samples is consistent with the aforementioned pattern of bacterial degradation. Similarly, some bacterial degradation of CFCs relative to SF_6 may be affecting AV(1), MA(5), and MZ(12) geothermal samples, which plot outside the atmospheric curve bounding area (Fig. 2.9b) and were under or near anaerobic conditions at the time of sampling (Table 2.1). Nonetheless, the consistently mismatching ages between the non-degrading SF_6 and CFC-12 (generally considered the most robust CFC under low-O_2 conditions) for geothermal samples, as well as the detectable presence of all tracers, evidence the addition of a small modern component to the hydrothermal fluid.

2.5.4 Conceptual model of fluid circulation

The geochemical, stable isotope, and anthropogenic tracer data presented in this study are integrated with the current understanding of the structural and geological arrangement of the SVZ, in order to derive a conceptual model of hydrothermal fluid source and circulation. This model is summarized in Figure 2.10.

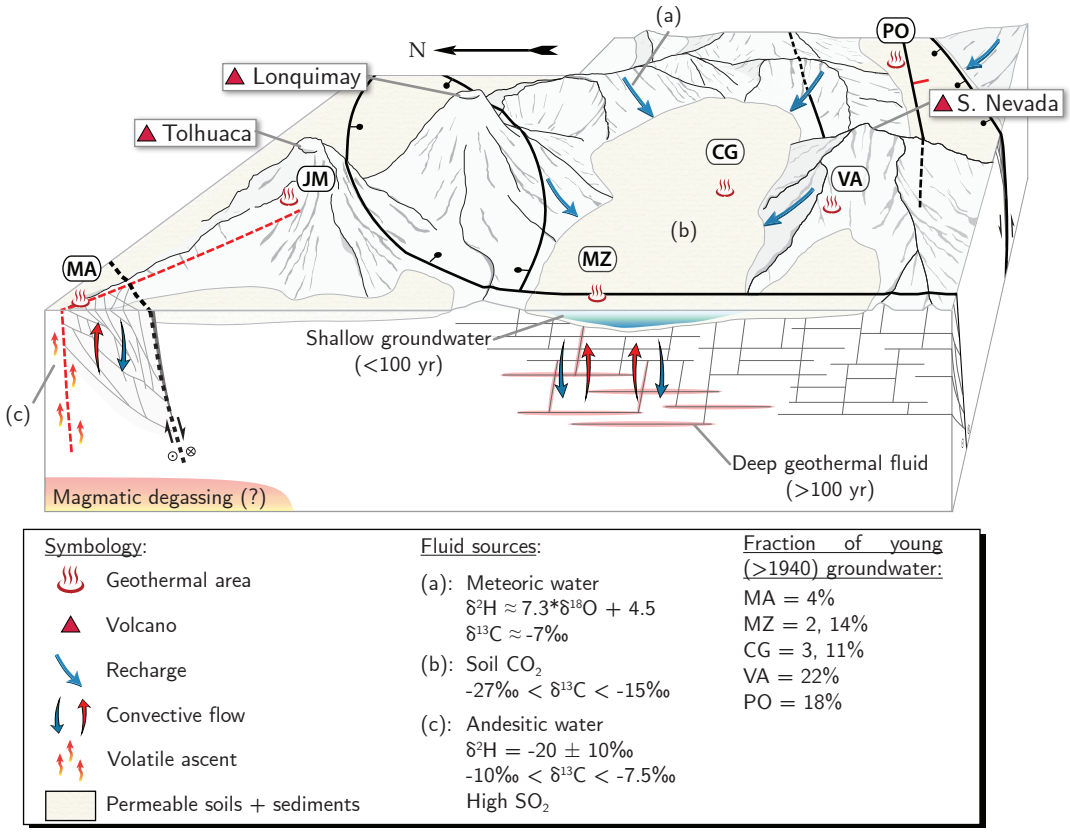

Figure 2.10: Conceptual model of hydrothermal fluid circulation proposed for the studied segment of the SVZ, indicating sources of fluid recharge (a, b, c) and mixing rates between young (<∼100 yr), shallow groundwater and old (>∼100 yr), deeply circulating geothermal fluid. Black and red lines represent the LOFS and the ATF, respectively, with associated damage zones shown in front profile. Andesitic water δ^2H values are taken from Giggenbach (1992). Geothermal areas PE and AV, located further north, are not shown.

In the Southern Volcanic Zone of Chile, west of the Andes, were topography is the dominant control on the distribution and isotope signature of precipitation, the bulk of rainfall occurs as air moisture is forced upwards along the steep slopes of volcanic arcs and mountains. In the area of the Lonquimay-Tolhuaca Volcanic Complex, δ^2H and δ^{18}O values of waters suggest that average recharge elevation of most thermal springs occurs at ∼1000–1200 m a.s.l., corresponding to the margins of valleys and lower flanks of mountain chains. Dissolution of soil CO_2 during the initial stages of infiltration is the primary source of C in waters, and imprints its C-isotope signature on the recharging fluid. Results from our modeling (Fig. 2.5) show that the addition of even small quantities of soil CO_2 significantly impacts $\delta^{13}C_{TDIC}$ values. In the vicinity of volcanic centers, an additional input of CO_2 of magmatic origin is detected in thermal waters associated with active fumarole fields.

Given the low intrinsic permeability of outcropping volcanic and plutonic units in the vicinity of the LTVC (Pérez-Flores et al., 2017b) fracture permeability plays a crucial role on the subsurface circulation of groundwater. Master and subsidiary faults of the LOFS splay off to the NE, developing extensional geometries, which constitute localized permeability pathways enhancing the vertical migration of fluids. Infiltrating groundwater penetrates deeper into the crust along these points of high secondary permeability. At greater depths, sandstones of the Río Pedregoso Fm. may have sufficient primary permeability to host a geothermal reservoir (Pedroza et al., 2017).

As water infiltrates deeper into the crust through fault-fracture networks, it becomes heated as a result of the increased geothermal gradient of the SVZ. Increased residence (and thus, reaction) times at higher temperatures induce greater degrees of fluid-rock interaction with the volcano-sedimentary rocks of the Malleco Fm. and Cura-Mallín Group, giving hydrothermal fluid its distinct geochemical composition from the recharging groundwater (Fig. 2.3). Magmatic degassing and boiling processes (samples MA(5-6), JM(7), BT(19) and VA(20)) are evidenced in samples discharging near volcanic systems. The initially soil-CO_2 dominated isotope signature of recharge to thermal systems is subsequently modified by fluid degassing and carbonate precipitation during ascent (Fig. 2.6 & 2.7). In this segment of the SVZ, calcite of hydrothermal origin has been observed in dilational jogs along master and subsidiary faults of the LOFS (Pérez-Flores et al., 2016), evidencing the occurrence of these processes, as well as the structurally-controlled migration of these fluids.

Focused flow along high vertical permeability pathways allows hydrothermal fluids to remain relatively unmixed with shallow meteoric waters, helping maintain elevated temperatures during their ascent to the surface. Nonetheless, low but detectable concentrations of anthropogenic tracers in all samples suggest the addition of a small fraction (2 to 22%) of downwards-percolating, modern meteoric fluid. Cold water is denser than hot water, and may have sufficient pressure to invade thermal aquifers at shallow depths (Truesdell et al., 1977). Mixing with cold meteoric fluids alters the geochemical composition of thermal fluids, induces carbonate precipitation, and partially resets any changes having occurred to the oxygen and hydrogen isotopic signatures at depth.

The above interpretation is consistent with the mechanisms of geothermal system formation described in Wrage et al. (2017), as well as the dissolved gas isotope data from Tardani et al. (2016), which concluded that the presence of crustal-scale fault systems promotes deep

circulation of meteoric fluids at $\sim 38°S$, masking any possible deep mantellic $\delta^{13}C_{CO_2}$ signature in thermal fluids due to shallow processes.

2.6 Concluding remarks

Results suggest that, in the vicinity of the LTVC, hydrothermal system recharge is sourced locally, and topography plays a fundamental role in its distribution. Variations in temperature of discharging springs correlate to different subsurface circulation pathways. These differences—for instance, the shallow, diffuse flow of cold groundwater vs. the deep, focused circulation of thermal water along fault zones—induce longer reaction times and increased subsurface P-T conditions, which in turn imprints hydrothermal fluids their distinct chemical signature due to fluid-rock interaction. Magmatic degassing and boiling processes play an important role near volcanic systems.

Binary mixing between an old, anthropogenic tracer-free fluid (hydrothermal waters) and a modern meteoric component (shallow groundwater) best describes the age distribution of naturally discharging thermal springs in the Southern Volcanic Zone. The modern meteoric groundwater fraction in these springs was measured to be between 2 and 22%. These low mixing fractions suggest the rapid ascent of an old, tracer-free fluid along focused pathways.

Data from this study confirm that the interplay between fault systems with different orientations exerts a first order control on the residence times, ascent, and mixing rates of thermal waters in this segment of the SVZ, thus modulating their chemical and isotopic signature. The ascent of geothermal fluids along favorably-oriented fault-fracture networks, and the dependence on these structures for deep groundwater circulation is consistent with previous studies in the SVZ (Sánchez et al., 2013; Pérez-Flores et al., 2016; Tardani et al., 2016; Pérez-Flores et al., 2017a,b; Roquer et al., 2017; Wrage et al., 2017). Our data proves that, despite similar recharge source, host lithology, and proximity of discharge points, residence times of thermal springs are fundamentally different from those of their non-thermal (or cold) counterparts, evidencing the different circulation pathways of these waters. Additionally, our results show that the combined use of conventional hydrogeochemical and isotopic data with environmental tracers, including anthropogenic CFC and SF_6, is a powerful tool to better understand the dynamics of geothermal systems in the Andes.

ACKNOWLEDGEMENTS

This study was funded by FONDAP project 15090013 "Centro de Excelencia en Geotermia de los Andes, CEGA". We acknowledge additional support by the Millennium Science Initiative (ICM) through grant #NC130065 "Millennium Nucleus for Metal Tracing along Subduction". We thank Dr. Harald Oster of the *Spurenstofflabor* for his swift and efficient work in tracer analysis, as well as Dr. Antonio Delgado Huertas at the Andalusian Institute of Earth Sciences (IACT) for his support with the analysis of stable isotopes. Appreciation is given to many landowners who kindly provided access to springs for sample collection.

CHAPTER 3: CONCLUSIONS

3.1 Scientific contributions of this dissertation

The results presented in this thesis provide new insights into the origin and evolution of fluids in a hydrothermal area of the Southern Volcanic Zone. In particular, this work contributes to our understanding on the role of fault-fracture meshes on residence times and the age distribution of fluids, along with the impact of shallow crustal processes (i.e. meteoric dilution, degassing) on their geochemical composition. The methods developed in this study may be applicable to other geothermal systems in the Andes, helping provide hydrogeological background knowledge useful to the development of geothermal exploration models. In addition, this work represents the first published measurements of dissolved SF_6 in groundwater in Chile, which was proven to be in low, but detectable, concentrations in all thermal samples at the Lonquimay-Tolhuaca Volcanic Complex.

The main conclusions of this work and the implications are summarized as follows:

- In the vicinity of the LTVC, hydrothermal system and cold groundwater recharge is sourced locally (i.e. within the same basin). The particular topography of the Andean Cordillera, which provides a crosswise barrier to the predominant wind direction, plays a fundamental role in modulating precipitation, and therefore, recharge distribution.

- The development of a local meteoric water line for this segment of the Andean arc (38–39°S), together with a mathematical model of the isotopic lapse rate in precipitation, allows for placing constraints on the recharge elevation of hydrothermal and cold groundwater systems in this area. The mathematical models are applicable to other groundwater/hydrothermal systems in the Araucanía region, and can be easily extended to other systems in the Andes, given sufficient data is available on the isotopic composition of precipitation.

- Magmatic degassing and boiling processes play an important role near volcanic systems (Tolhuaca and Sierra Nevada), and are likely related to volatile ascent through the ATF. This is consistent with the tectonic-magmatic-hydrothermal domains defined in previous studies, as the misorientation of the ATF with regard to the present day stress-regime favors magmatic chamber development, differentiation, and subsequent degassing.

- Residence times and age distribution of thermal springs are fundamentally different than those of their non-thermal (or cold) counterparts, evidencing the different circulation pathways of these waters. Cold springs possess shorter residence times and varying degrees of fluid mixing. Thermal waters evidence longer residence times, and remain relatively unmixed. Longer residence times, in turn, induce longer reaction times at increased subsurface P-T conditions, imprinting hydrothermal fluid with its distinct chemical signature due to fluid-rock interaction.

- Binary mixing between an old, anthropogenic tracer-free waters (hydrothermal fluid) and a modern meteoric component (shallow groundwater) best describes the age distribution of naturally discharging thermal springs in this area of the Southern Volcanic Zone. The modern meteoric groundwater fraction in these springs was measured to be between 2–22%. These low mixing fractions suggest the rapid ascent of an old, tracer-free fluid along focused pathways.

- The effects of meteoric dilution in hydrothermal fluid (i.e., mixing of hydrothermal fluid with cold meteoric water during ascent) were constrained to be less than 22%. There was no systematic difference detected between ATF and LOFS associated systems, although springs discharging in valleys over permeable Quaternary sediment (MZ, CG, PO) tend to be more diluted than springs discharging in the flanks of volcanoes or fractured intrusive rock (MA, PE, AV). It must be considered, however, that the precise fraction of modern groundwater in a given spring is highly dependent on local outflow conditions, such as the presence of nearby rivers, streams, or shallow groundwater bodies. The dilution percentage may present seasonal variations as well. For example, dilution with shallow groundwater might increase during rainier periods. Systematic measurements throughout the year must be carried out to precisely determine these effects.

- Results from this study confirm that fault systems with different orientations exert a first order control on the residence times, ascent, and mixing rates of thermal waters in this segment of the SVZ, thus modulating their chemical and isotopic signature. The ascent of geothermal fluids through favorably-oriented fault-fracture networks, and the dependence on these structures for deep groundwater circulation is consistent with previous studies in the SVZ.

- Our results show that the combined use of conventional hydrogeochemical and isotopic data with environmental tracers, including anthropogenic CFC and SF_6, is a powerful tool to better understand the dynamics of geothermal systems.

3.2 Future work

Results from this thesis provide hydrogeological background knowledge that, compounded with experimental permeability data, can be used in more detailed studies and provide key boundary conditions for hydrological model simulations to: quantify recharge area of groundwater systems, estimate recharge rates, flow velocities, water balance, etc.

One of the main limitations of hydrogeological research in Chile is the lack of basic hydrogeological data. Efforts should be undertaken to constrain the isotope signature of precipitation and groundwater at different altitudes and different times of the year, at a basin level. Precisely constraining the age of thermal waters will require the use of multiple tracers with different age ranges. Although all tracers have inherent drawbacks (for example, ^{14}C in geothermal systems is complicated by additional sources of magmatic carbon, or calcite precipitation), this study has shown that the multi-tracer approach can circumvent these limitations and increase robustness of groundwater dating results.

Bibliography

American Meteorological Society (2018). AMS Glossary of Meteorology. [On-line] http://glossary.ametsoc.org/wiki/Main_Page. Last accessed on 27/03/2019.

Angermann, D., Klotz, J., and Reigber, C. (1999). Space-geodetic estimation of the Nazca-South America Euler vector. *Earth and Planetary Science Letters*, 171(3):329–334.

Appelo, C. and Postma, D. (2005). *Geochemistry, Groundwater and Pollution*. A.A. Balkema Publishers, Leiden, The Netherlands.

Aravena, D., Muñoz, M., Morata, D., Lahsen, A., Parada, M. Á., and Dobson, P. (2016). Assessment of high enthalpy geothermal resources and promising areas of Chile. *Geothermics*, 59:1–13.

Arnórsson, S. (1995). Geothermal systems in Iceland: Structure and conceptual models—I. High-temperature areas. *Geothermics*, 24:561–602.

Arnórsson, S., Stefansson, A., and Bjarnason, J. O. (2007). Fluid-Fluid Interactions in Geothermal Systems. *Reviews in Mineralogy and Geochemistry*, 65(1):259–312.

Benjamin, L., Knobel, L. L., Hall, L. F., Cecil, L. D., and Green, J. R. (2005). Development of a Local Meteoric Water Line for Southeastern Idaho , Western Wyoming , and South-Central Montana. U.S. Geological Survey.

Bu, X. and Warner, M. J. (1995). Solubility of chlorofluorocarbon 113 in water and seawater. *Deep Sea Research Part I: Oceanographic Research Papers*, 42(7):1151–1161.

Buck, A. L. (1981). New Equations for Computing Vapor Pressure and Enhancement Factor. *Journal of Applied Meteorology*, 20(12):1527–1532.

Bullister, J. (2015). Atmospheric Histories (1765–2015) for CFC-11, CFC-12, CFC-113, CCl_4, SF_6 and N_2O. National Oceanic and Atmospheric Administration. [On-line] https://www.nodc.noaa.gov/ocads/oceans/CFC_ATM_Hist2015.html. Last accessed on 27/03/2019.

Bullister, J. and Weiss, R. (1988). Determination of CCl3F and CCl2F2 in seawater and air. *Deep Sea Research Part A. Oceanographic Research Papers*, 35(5):839–853.

Bullister, J. L., Wisegarver, D. P., and Menzia, F. A. (2002). The solubility of sulfur hexafluoride in water and seawater. *Deep Sea Research Part I: Oceanographic Research Papers*, 49(1):175–187.

Burns, W. M., Jordan, T. E., Copeland, P., and Kelley, S. A. (2006). The case for extensional tectonics in the Oligocene-Miocene Southern Andes as recorded in the Cura Mallín basin (36°–38°S). *Geological Society of America Special Papers*, 407:163–184.

Busenberg, E. and Plummer, L. (2006). Potential use of other atmospheric gases. In *Use of*

Chlorofluorocarbons in Hydrology, chapter 11, pages 183–190. International Atomic Energy Agency.

Busenberg, E., Plummer, L., Cook, P., Solomon, D., Han, L., Gröning, M., and Oster, H. (2006). Sampling and analytical methods. In *Use of Chlorofluorocarbons in Hydrology*, chapter 12, pages 199–220. International Atomic Energy Agency.

Cathles, L. M., Erendi, A. H. J., and Barrie, T. (1997). How long can a hydrothermal system be sustained by a single intrusive event? *Economic Geology*, 92(7-8):766–771.

Cembrano, J., Hervé, F., and Lavenu, A. (1996). The Liquiñe Ofqui fault zone: a long-lived intra-arc fault system in southern Chile. *Tectonophysics*, 259:55–66.

Cembrano, J. and Lara, L. (2009). The link between volcanism and tectonics in the southern volcanic zone of the Chilean Andes: A review. *Tectonophysics*, 471:96–113.

Cerling, T. E. (1984). The stable isotopic composition of modern soil carbonate and its relationship to climate. *Earth and Planetary Science Letters*.

Chiodini, G., Frondini, F., Cardellini, C., Parello, F., and Peruzzi, L. (2000). Rate of diffuse carbon dioxide Earth degassing estimated from carbon balance of regional aquifers: The case of central Apennine, Italy. *Journal of Geophysical Research: Solid Earth*.

Clark, I. and Fritz, P. (1997). *Environmental Isotopes in Hydrology*. CRC Press, Boca Raton.

Cook, P., Plummer, L., Solomon, D., Busenberg, E., and Han, L. (2006). Effects and processes that can modify apparent CFC age. In *Use of Chlorofluorocarbons in Hydrology*, chapter 4, pages 31–58. International Atomic Energy Agency.

Craig, H. (1963). *The Isotopic Geochemistry of Water and Carbon in Geothermal Areas*. Consiglio Nazionale Delle Ricerche (CNR), Laboratorio Di Geologia Nucleare, Pisa, Italy.

Cusicanqui, H. (1979). *Estudio geoquímico del área termal se Surire, provincia de Arica, I Región*. Technical report, Comité Geotérmico CORFO.

Dansgaard, W. (1964). Stable isotopes in precipitation. *Tellus*, 16(4):436–368.

Darling, W., Gooddy, D., MacDonald, A., and Morris, B. (2012). The practicalities of using CFCs and SF_6 for groundwater dating and tracing. *Applied Geochemistry*, 27(9):1688–1697.

Deines, P., Langmuir, D., and Harmon, R. (1974). Stable carbon isotope ratios and the existence of a gas phase in the evolution of carbonate ground waters. *Geochimica et Cosmochimica Acta*, 38(7):1147–1164.

Deipser, A. and Stegmann, R. (1997). Biological degradation of VCCs and CFCs under simulated anaerobic landfill conditions in laboratory test digesters. *Environmental Science and Pollution Research*.

Dirección General de Aguas (2016). *Estudio Hidrogeológico, Región de la Araucanía*. Tech-

nical report, Dirección General de Aguas.

Druschel, G. K. and Rosenberg, P. E. (2001). Non-magmatic fracture-controlled hydrothermal systems in the Idaho Batholith: South Fork Payette geothermal system. *Chemical Geology*, 173:271–291.

Edmunds, W. M., Darling, W. G., Purtschert, R., and Corcho Alvarado, J. A. (2014). Noble gas, CFC and other geochemical evidence for the age and origin of the Bath thermal waters, UK. *Applied Geochemistry*, 40:155–163.

Elkins, J. W., Thompson, T. M., Swanson, T. H., Butler, J. H., Hall, B. D., Cummings, S. O., Fishers, D. A., and Raffo, A. G. (1993). Decrease in the growth rates of atmospheric chlorofluorocarbons 11 and 12. *Nature*, 364:780–783.

Ellis, A. and Mahon, W. (1977). *Chemistry and geothermal systems.* Academic press, New York.

Faulkner, D. R., Jackson, C. A., Lunn, R. J., Schlische, R. W., Shipton, Z. K., Wibberley, C. A., and Withjack, M. O. (2010). A review of recent developments concerning the structure, mechanics and fluid flow properties of fault zones. *Journal of Structural Geology*, 32:1557–1575.

Fernández, A., Muñoz, A., González-Reyes, Á., Aguilera-Betti, I., Toledo, I., Puchi, P., Sauchyn, D., Crespo, S., Frene, C., Mundo, I., González, M., and Vignola, R. (2018). Dendrohydrology and water resources management in south-central Chile: lessons from the Río Imperial streamflow reconstruction. *Hydrology and Earth System Sciences*, 22(5):2921–2935.

Frondini, F., Caliro, S., Cardellini, C., Chiodini, G., and Morgantini, N. (2009). Carbon dioxide degassing and thermal energy release in the Monte Amiata volcanic-geothermal area (Italy). *Applied Geochemistry*, 24(5):860–875.

Gamlen, P., Lane, B., Midgley, P., and Steed, J. (1986). The production and release to the atmosphere of CCl3F and CCl2F2 (chlorofluorocarbons CFC 11 and CFC 12). *Atmospheric Environment (1967)*, 20(6):1077–1085.

Gardner, W. P., Susong, D. D., Solomon, D. K., and Heasler, H. P. (2011). A multitracer approach for characterizing interactions between shallow groundwater and the hydrothermal system in the Norris Geyser Basin area, Yellowstone National Park. *Geochemistry, Geophysics, Geosystems*, 12(8).

Garreaud, R. D. (2009). The Andes climate and weather. *Advances in Geosciences*, 22:3–11.

Giggenbach, W. (1992). Isotopic shifts in waters from geothermal and volcanic systems along convergent plate boundaries and their origin. *Earth and Planetary Science Letters*, 113(4):495–510.

Giggenbach, W. F. (1988). Geothermal solute equilibria. Derivation of Na-K-Mg-Ca geoindicators. *Geochimica et Cosmochimica Acta*, 52(12):2749–2765.

Giggenbach, W. F. (1997). The origin and evolution of fluids in magmatic-hydrothermal systems. In *Geochemistry of hydrothermal ore deposits*, chapter 15, pages 736–789. John Wiley and Sons, Inc.

Giggenbach, W. F. and Gougel, R. (1989). Collection and analysis of geothermal and volcanic water and gas discharges. Technical report, Chemistry Division, Department of Scientific and Industrial Research, Petone, New Zealand.

Hansen, J., Lacis, A., and Prather, M. (1989). Greenhouse effect of chlorofluorocarbons and other trace gases. *Journal of Geophysical Research*, 94(D13):16417.

Happell, J., Wallace, D., Wills, K., Wilke, R., and Neill, C. (1996). A purge-and-trap capillary column gas chromatographic method for the measurement of halocarbons in water and air. Technical report, Brookhaven National Laboratory (BNL), Upton, NY (United States).

Hauser, A. (1997). *Catastro y Caracterización de las Fuentes de Aguas Minerales y Termales de Chile: Servicio Nacional de Geología y Minería*. Boletín, v. 50, p. 90.

Hedenquist, J. W. (1991). Boiling and dilution in the shallow portion of the Waiotapu geothermal system, New Zealand. *Geochimica et Cosmochimica Acta*, 55(10):2753–2765.

Held, S., Nitschke, F., Schill, E., Morata, D., Eiche, E., and Kohl, T. (2017). Hydrochemistry of the hot spring fluids of Villarrica geothermal system in the Andes of Southern Chile. In *GRC Transactions*, volume 41.

Held, S., Schill, E., Schneider, J., Nitschke, F., Morata, D., Neumann, T., and Kohl, T. (2018). Geochemical characterization of the geothermal system at Villarrica volcano, Southern Chile; Part 1: Impacts of lithology on the geothermal reservoir. *Geothermics*, 74:226–239.

Horita, J. and Wesolowski, D. J. (1994). Liquid-vapor fractionation of oxygen and hydrogen isotopes of water from the freezing to the critical temperature. *Geochimica et Cosmochimica Acta*, 58:3425–3437.

Horneman, A., Stute, M., Schlosser, P., Smethie, W., Santella, N., Ho, D., Mailloux, B., Gorman, E., Zheng, Y., and van Geen, A. (2008). Degradation rates of CFC-11, CFC-12 and CFC-113 in anoxic shallow aquifers of Araihazar, Bangladesh. *Journal of Contaminant Hydrology*, 97(1-2):27–41.

IAEA/WMO (2018). Global Network of Isotopes in Precipitation. The GNIP Database. [On-line] https://nucleus.iaea.org/wiser. Last accessed on 27/03/2019.

Insel, N., Poulsen, C. J., and Ehlers, T. A. (2010). Influence of the Andes Mountains on South American moisture transport, convection, and precipitation. *Climate Dynamics*, 35(7-8):1477–1492.

Intergovermental Panel on Climate Change (1995). IPCC Second Assessment: Climate Change 1995, Summary for Policymakers and Technical Summary of the Working Group I Report, Climate Change, UNEP/WMO, Nairobi.

ISO (1975). Standard Atmosphere, ISO 2533:1975. Technical report, International Organization for Standardization.

James, E., Manga, M., Rose, T., and Hudson, G. (2000). The use of temperature and the isotopes of O, H, C, and noble gases to determine the pattern and spatial extent of groundwater flow. *Journal of Hydrology*, 237(1-2):100–112.

Kaasalainen, H. and Stefánsson, A. (2012). The chemistry of trace elements in surface geothermal waters and steam, Iceland. *Chemical Geology*, 330-331:60–85.

Kelly, J. L. and Glenn, C. R. (2015). Chlorofluorocarbon apparent ages of groundwaters from west Hawaii, USA. *Journal of Hydrology*, 527:355–366.

Khalil, M. A. K. and Rasmussen, R. A. (1989). The potential of soils as a sink of chlorofluorocarbons and other man-made chlorocarbons. *Geophysical Research Letters*, 16(7):679–682.

Kroeze, C. and Reijnders, L. (1992). Halocarbons and global warming. *Science of The Total Environment*, 111(1):1–24.

Lahsen, A. (1976). Geothermal exploration in Northern Chile – summary. In *Circum-Pacific Energy and Mineral Resources*, pages 169–175. The American Association of petroleum Geologists.

Lahsen, A. (1978). *Evaluación de los resultados de la exploración del campo geotérmico de Puchildiza, I Región de Tarapacá*. Technical report, Comité Geotérmico CORFO.

Lahsen, A. (1988). Chilean geothermal resources and their possible utilization. *Geothermics*, 17(2-3):401–410.

Lahsen, A., Muñoz, N., and Parada, M. A. (2010). Geothermal Development in Chile. In *Proceedings World Geothermal Congress*, Bali, pp. 25–29.

Lara, L. E., Lavenu, A., Cembrano, J., and Rodríguez, C. (2006). Structural controls of volcanism in transversal chains: Resheared faults and neotectonics in the Cordón Caulle-Puyehue area (40.5°S), Southern Andes. *Journal of Volcanology and Geothermal Research*, 158:70–86.

Letelier, M. (1981). *Geoquímica de las manifestaciones termales de Puchuldiza y sus alrededores*. Technical report, Comité Geotérmico CORFO.

Lopez-Escobar, L., Cembrano, J., and Moreno, H. (1995). Geochemistry and tectonics of the Chilean southern Andes basaltic Quaternary volcanism (37–46°S). *Revista Geologica de Chile*, 22:219–234.

Maiss, M. and Brenninkmeijer, C. A. M. (1998). Atmospheric SF_6: Trends, Sources, and Prospects. *Environmental Science & Technology*, 32(20):3077–3086.

Majoube, M. (1970). Fractionation factor of ^{18}O between water vapour and ice. *Nature*, 226:1242.

Małoszewski, P. and Zuber, A. (1982). Determining the turnover time of groundwater systems with the aid of environmental tracers. *Journal of Hydrology*, 57(3-4):207–231.

Manning, C. E. and Ingebritsen, S. E. (1999). Permeability of the continental crust: Implications of geothermal data and metamorphic systems. *Reviews of Geophysics*, 37(1):127–150.

Melnick, D., Folguera, A., and Ramos, V. A. (2006). Structural control on arc volcanism: The Caviahue-Copahue complex, Central to Patagonian Andes transition (38°S). *Journal of South American Earth Sciences*, 22:66–88.

Melosh, G., Cumming, W., Benoit, D., Wilmarth, M., Colvin, A., Winick, J., Soto-Neira, E., Sussman, D., Urzúa-Monsalve, L., Powell, T., and Peretz, A. (2010). Exploration results and resource conceptual model of the Tolhuaca Geothermal Field, Chile. In *Proceedings World Geothermal Congress*, pages 25–29.

Melosh, G., Moore, J., and Stacey, R. (2012). Natural reservoir evolution in the Tolhuaca geothermal field, southern Chile. In *Thirty-Sixth Workshop on Geothermal Reservoir Engineering*, pages Stanford, California, January 30 – February 1, 201.

Midgley, P. and Fisher, D. (1993). The production and release to the atmosphere of chlorodifluoromethane (HCFC 22). *Atmospheric Environment. Part A. General Topics*, 27(14):2215–2223.

Moeck, I. S. (2014). Catalog of geothermal play types based on geologic controls. *Renewable and Sustainable Energy Reviews*, 37:867–882.

Molina, M. J. and Rowland, F. S. (1974). Stratospheric sink for chlorofluoromethanes: chlorine atom-catalysed destruction of ozone. *Nature*, 249(5460):810–812.

Muñoz, M., Ayaz Alam, M., Parada, M. Á., and Lahsen, A. (2011). Geothermal System Associated with the Sierra Nevada Volcano, Araucanía Region, Chile. *GRC Transactions*, 35:935–941.

Negri, A., Daniele, L., Aravena, D., Muñoz, M., Delgado, A., and Morata, D. (2018). Decoding fjord water contribution and geochemical processes in the Aysen thermal springs (Southern Patagonia, Chile). *Journal of Geochemical Exploration*, 185:1–13.

Niemeyer, H. and Muñoz, J. (1983). *Geología de la hoja Laguna de la Laja: Región del Bio-Bio, escala 1:250.000. Carta geológica de Chile. Servicio Nacional de Geología y Minería.*

Oehlert, A. M. and Swart, P. K. (2014). Interpreting carbonate and organic carbon isotope covariance in the sedimentary record. *Nature Communications*, 5(1):4672.

Oster, H., Sonntag, C., and Münnich, K. O. (1996). Groundwater age dating with chlorofluorocarbons. *Water Resources Research*, 32(10):2989–3001.

Pardo-Casas, F. and Molnar, P. (1987). Relative motion of the Nazca (Farallon) and South American Plates since Late Cretaceous time. *Tectonics*, 6(3):233–248.

Parkhurst, D. L. and Appelo, C. A. J. (2013). Description of input and examples for PHREEQC Version 3 — A computer program for speciation, batch-reaction, one-dimensional transport, and inverse geochemical calculations. *U.S. Geological Survey Techniques and Methods, book 6, chapter A43*, page 497.

Pedroza, V., Le Roux, J. P., Gutiérrez, N. M., and Vicencio, V. E. (2017). Stratigraphy, sedimentology, and geothermal reservoir potential of the volcaniclastic Cura-Mallín succession at Lonquimay, Chile. *Journal of South American Earth Sciences*, 77:1–20.

Pérez-Flores, P., Cembrano, J., Sánchez-Alfaro, P., Veloso, E., Arancibia, G., and Roquer, T. (2016). Tectonics, magmatism and paleo-fluid distribution in a strike-slip setting: Insights from the northern termination of the Liquiñe-Ofqui fault System, Chile. *Tectonophysics*, 680:192–210.

Pérez-Flores, P., Veloso, E., Cembrano, J., Sánchez-Alfaro, P., Lizama, M., and Arancibia, G. (2017a). Fracture network, fluid pathways and paleostress at the Tolhuaca geothermal field. *Journal of Structural Geology*, 96:134–148.

Pérez-Flores, P., Wang, G., Mitchell, T. M., Meredith, P. G., Nara, Y., Sarkar, V., and Cembrano, J. (2017b). The effect of offset on fracture permeability of rocks from the Southern Andes Volcanic Zone, Chile. *Journal of Structural Geology*, 104:142–158.

Plummer, L. and Busenberg, E. (2006). Chlorofluorocarbons in aquatic environments. In *Use of Chlorofluorocarbons in Hydrology*, chapter 1, pages 1–8. International Atomic Energy Agency.

Plummer, L., Busenberg, E., and Cook, P. (2006a). Principles of Chlorfluorocarbon dating. In *Use of Chlorofluorocarbons in Hydrology*, chapter 3, pages 17–29. International Atomic Energy Agency.

Plummer, L., Busenberg, E., and Han, L. (2006b). CFCs in Binary Mixtures of Young and Old Groundwater. In *Use of Chlorofluorocarbons in Hydrology*, chapter 5, pages 59–72. International Atomic Energy Agency.

Radic, J. P. (2010). Las cuencas cenozoicas y su control en el volcanismo de los Complejos Nevados de Chillán y Copahue-Callaqui (Andes del sur, 36–39°S). *Andean Geology*, 37:220–246.

Ray, M. C., Hilton, D. R., Muñoz, J., Fischer, T. P., and Shaw, A. M. (2009). The effects of volatile recycling, degassing and crustal contamination on the helium and carbon geochemistry of hydrothermal fluids from the Southern Volcanic Zone of Chile. *Chemical Geology*, 266(1-2):38–49.

Reynolds, G. W., Hoff, J. T., and Gillham, R. W. (1990). Sampling Bias Caused by Materials Used To Monitor Halocarbons in Groundwater. *Environmental Science and Technology*, 24(1):135–142.

Rightmire, C. T. and Hanshaw, B. B. (1973). Relationship between the carbon isotope composition of soil CO 2 and dissolved carbonate species in groundwater. *Water Resources*

Research, 9(4):958–967.

Rolker, J., Schill, E., Stober, I., Schneider, J., Neumann, T., and Kohl, T. (2015). Hydrochemical characterisation of a major central European heat flux anomaly: the Bürchau geothermal spring system, Southern Black Forest, Germany. *Geothermal Energy*, 3:5.

Roquer, T., Arancibia, G., Rowland, J., Iturrieta, P., Morata, D., and Cembrano, J. (2017). Fault-controlled development of shallow hydrothermal systems: Structural and mineralogical insights from the Southern Andes. *Geothermics*, 66:156–173.

Rose, T. P. and Davisson, M. L. (1996). Radiocarbon in hydrologic systems containing dissolved magmatic carbon dioxide. *Science*, 273:1367–1370.

Rosenau, M., Melnick, D., and Echtler, H. (2006). Kinematic constraints on intra-arc shear and strain partitioning in the southern Andes between 38°S and 42°S latitude. *Tectonics*, 25:1–16.

Rowland, J. V. and Sibson, R. H. (2004). Structural controls on hydrothermal flow in a segmented rift system, Taupo Volcanic Zone, New Zealand. *Geofluids*, 4(4):259–283.

Rowley, D. B. (2007). Stable Isotope-Based Paleoaltimetry: Theory and Validation. *Reviews in Mineralogy and Geochemistry*, 66:23–52.

Rowley, D. B., Pierrehumbert, R. T., and Currie, B. S. (2001). A new approach to stable isotope-based paleoaltimetry: implications for paleoaltimetry and paleohypsometry of the High Himalaya since the Late Miocene. *Earth and Planetary Science Letters*, 188(1-2):253–268.

Rozanski, K. and Araguás-Araguás, L. (1995). Spatial and temporal variability of stable isotope composition of precipitation over the South American continent. *Bulletin de l'Institut francais d'etudes andines*, 24:379–390.

Rozanski, K., Araguás-Araguás, L., and Gonfiantini, R. (1993). Isotopic Patterns in Modern Global Precipitation. In *Climate Change in Continental Isotopic Records*, pages 1–36. American Geophysical Union, Washington.

Sánchez, P., Pérez-Flores, P., Arancibia, G., Cembrano, J., and Reich, M. (2013). Crustal deformation effects on the chemical evolution of geothermal systems: The intra-arc Liquiñe-Ofqui fault system, Southern Andes. *International Geology Review*, 55:1384–1400.

Sanchez-Alfaro, P., Reich, M., Arancibia, G., Pérez-Flores, P., Cembrano, J., Driesner, T., Lizama, M., Rowland, J., Morata, D., Heinrich, C. A., Tardani, D., and Campos, E. (2016). Physical, chemical and mineralogical evolution of the Tolhuaca geothermal system, southern Andes, Chile: Insights into the interplay between hydrothermal alteration and brittle deformation. *Journal of Volcanology and Geothermal Research*, 324:88–104.

Sanchez-Alfaro, P., Sielfeld, G., Campen, B. V., Dobson, P., Fuentes, V., Reed, A., Palma-Behnke, R., and Morata, D. (2015). Geothermal barriers, policies and economics in Chile – Lessons for the Andes. *Renewable and Sustainable Energy Reviews*, 51:1390–1401.

Sano, Y. and Marty, B. (1995). Origin of carbon in fumarolic gas from island arcs. *Chemical Geology*, 119(1-4):265–274.

Sebol, L., Robertson, W., Busenberg, E., Plummer, L., Ryan, M., and Schiff, S. (2007). Evidence of CFC degradation in groundwater under pyrite-oxidizing conditions. *Journal of Hydrology*, 347(1-2):1–12.

Seluchi, M., Serafini, Y. V., and Le Treut, H. (1998). The Impact of the Andes on Transient Atmospheric Systems: A Comparison between Observations and GCM Results. *Monthly Weather Review*, 126(4):895–912.

Semprini, L., Hopkins, G. D., McCarty, P. L., and Roberts, P. V. (1992). In-situ transformation of carbon tetrachloride and other halogenated compounds resulting from biostimulation under anoxic conditions. *Environmental Science & Technology*, 26(12):2454–2461.

Sibson, R. H. (1996). Structural permeability of fluid-driven fault-fracture meshes. *Journal of Structural Geology*, 18(8):1031–1042.

Soffia, J. and Clavero, J. (2010). Doing geothermal exploration business in Chile, Energía Andina experience. In *Transactions - Geothermal Resources Council*.

Somoza, R. (1998). Updated Nazca (Farallon)-South America relative motions during the last 40 My: Implications for mountain building in the central Andean region. *Journal of South American Earth Sciences*, 11:211–215.

Stern, L. A. and Blisniuk, P. M. (2002). Stable isotope composition of precipitation across the southern Patagonian Andes. *Journal of Geophysical Research: Atmospheres*, 107(D23).

Stöwhas, L. and Moyano, J. C. (1993). Simulation of the isotopic content of precipitation. *Atmospheric Environment. Part A. General Topics*, 27(3):327–333.

Suárez, M. and Emparan, C. (1997). *Hoja Curacautín, región de la Araucanía y del Biobío. Carta Geológica de Chile*. Servicio Nacional de Geología y Minería.

Suckow, A. (2014). The age of groundwater – Definitions, models and why we do not need this term. *Applied Geochemistry*, 50:222–230.

Tardani, D., Reich, M., Roulleau, E., Takahata, N., Sano, Y., Pérez-Flores, P., Sánchez-Alfaro, P., Cembrano, J., and Arancibia, G. (2016). Exploring the structural controls on helium, nitrogen and carbon isotope signatures in hydrothermal fluids along an intra-arc fault system. *Geochimica et Cosmochimica Acta*, 184:193–211.

Taylor, J. R. (1997). *An introduction to error analysis: The study of uncertainties in physical measurements, 2d ed.* University Science Books, Sausalito, Calif. (United States).

Truesdell, A. H., Nathenson, M., and Rye, R. O. (1977). The effects of subsurface boiling and dilution on the isotopic compositions of Yellowstone thermal waters. *Journal of Geophysical Research*, 82(26):3694–3704.

Upstill-Goddard, R. C. and Wilkins, C. S. (1995). The potential of SF_6 as a geothermal tracer. *Water Research*, 29:1065–1068.

Vicencio, V. (2015). *Geología y mineralogía de alteración en una sucesión volcano-sedimentaria en la Zona Volcánica Sur Central, Chile. Evidencias de un paleo-sistema volcánico y geotermal en la Formación Cura-Mallín.* In *Congreso Geológico Chileno No. 14, Actas.*

Vogel, J. (1970). Carbon-14 dating of groundwater. In *Isotope hydrology*, pages 225–240. International Atomic Energy Agency.

Walker, S. J., Weiss, R. F., and Salameh, P. K. (2000). Reconstructed histories of the annual mean atmospheric mole fractions for the halocarbons CFC-11 CFC-12, CFC-113, and carbon tetrachloride. *Journal of Geophysical Research: Oceans*, 105(C6):14285–14296.

Wallace, J. M. and Hobbs, P. V. (2006). *Atmospheric Science: An Introductory Survey: Second Edition.* Academic Press.

Warner, M. J. and Weiss, R. F. (1985). Solubilities of chlorofluorocarbons 11 and 12 in water and seawater. *Deep Sea Research Part A, Oceanographic Research Papers.*

Weiss, R. and Price, B. (1980). Nitrous oxide solubility in water and seawater. *Marine Chemistry*, 8(4):347–359.

Wrage, J., Tardani, D., Reich, M., Daniele, L., Arancibia, G., Cembrano, J., Sánchez-Alfaro, P., Morata, D., and Pérez-Moreno, R. (2017). Geochemistry of thermal waters in the Southern Volcanic Zone, Chile – Implications for structural controls on geothermal fluid composition. *Chemical Geology*, 466:545–561.

Zhang, J., Quay, P., and Wilbur, D. (1995). Carbon isotope fractionation during gas-water exchange and dissolution of CO_2. *Geochimica et Cosmochimica Acta*, 59(1):107–114.

Appendix A – Supplementary material

A.3 Data for constructing the local meteoric water line

Table A.1: Isotope precipitation data from the Araucanía Region, Southern Chile.

ID	Source	Location			Sampling period		Precip.	Temp.	δ^{18}O	δ^{2}H			
		Latitude	Longitude	m a.s.l	Start	Finish	[mm]	[°C]	[‰]	[‰]	d-excess	Outlier	Residual
198810	GNIP - Temuco	-38.732639	-72.589222	114	1988/10/01	1988/10/31	99	9.2	-5.6	-44	0.8	No	1.4
198902	GNIP - Temuco	-38.732639	-72.589222	114	1989/02/01	1989/02/28	17	16.2	-4.3	-28	6.4	No	7.9
198903	GNIP - Temuco	-38.732639	-72.589222	114	1989/03/01	1989/03/31	44	13	-6.3	-44	6.4	No	6.5
198904	GNIP - Temuco	-38.732639	-72.589222	114	1989/04/01	1989/04/30	23	10.6	-2.7	-18	3.6	No	6.2
198905	GNIP - Temuco	-38.732639	-72.589222	114	1989/05/01	1989/05/31	50	7.9	-9.0	-55	17	No	15.3
198906	GNIP - Temuco	-38.732639	-72.589222	114	1989/06/01	1989/06/30	234	8.2	-7.8	-60	2.4	No	1.5
198907	GNIP - Temuco	-38.732639	-72.589222	114	1989/07/01	1989/07/31	158	7.3	-8.7	-60	9.6	No	8.1
198908	GNIP - Temuco	-38.732639	-72.589222	114	1989/08/01	1989/08/31	140	7.8	-8.5	-65	3	No	1.6
198911	GNIP - Temuco	-38.732639	-72.589222	114	1989/11/01	1989/11/30	21	13.1	-8.3	-42	24.4	Yes	
198912	GNIP - Temuco	-38.732639	-72.589222	114	1989/12/01	1989/12/31	112	15.7	-7.7	-50	11.6	No	10.8
199003	GNIP - Temuco	-38.732639	-72.589222	114	1990/03/01	1990/03/31	103	13.3	-7.4	-53	6.2	No	5.6
199004	GNIP - Temuco	-38.732639	-72.589222	114	1990/04/01	1990/04/30	71	10.2	-5.8	-43	3.4	No	3.9
199005	GNIP - Temuco	-38.732639	-72.589222	114	1990/05/01	1990/05/31	172	8.8	-5.9	-34	13.2	No	13.6
199006	GNIP - Temuco	-38.732639	-72.589222	114	1990/06/01	1990/06/30	155	6.9	-4.8	-37	1.4	No	2.6
199007	GNIP - Temuco	-38.732639	-72.589222	114	1990/07/01	1990/07/31	97	6.9	-5.8	-50	-3.6	Yes	
199010	GNIP - Temuco	-38.732639	-72.589222	114	1990/10/01	1990/10/31	50	10.6	-9.4	-66	9.2	No	7.2
199011	GNIP - Temuco	-38.732639	-72.589222	114	1990/11/01	1990/11/30	45	11.5	-6.1	-34	14.8	No	15.1
199012	GNIP - Temuco	-38.732639	-72.589222	114	1990/12/01	1990/12/31	17	14	-5.3	-28	14.4	No	15.2
199101	GNIP - Temuco	-38.732639	-72.589222	114	1991/01/01	1991/01/31	38	15.6	-5.9	-40	7.2	No	7.6
199102	GNIP - Temuco	-38.732639	-72.589222	114	1991/02/01	1991/02/28	9	15.5	-7.2	-48	9.6	No	9.1
199104	GNIP - Temuco	-38.732639	-72.589222	114	1991/04/01	1991/04/30	153	10.7	-8.4	-55	12.2	No	10.9
199105	GNIP - Temuco	-38.732639	-72.589222	114	1991/05/01	1991/05/31	240	8.9	-8.1	-56	8.8	No	7.7

Table A.1: (continued)

		Location			Sampling period		Precip.	Temp.	δ^{18}O	δ^{2}H			
ID	Source	Latitude	Longitude	m a.s.l	Start	Finish	[mm]	[°C]	[‰]	[‰]	d-excess	Outlier	Residual
199106	GNIP - Temuco	-38.732639	-72.589222	114	1991/06/01	1991/06/30	128	7.2	-8.6	-63	5.8	No	4.6
199107	GNIP - Temuco	-38.732639	-72.589222	114	1991/07/01	1991/07/31	198	7.1	-7.1	-50	6.8	No	6.4
199108	GNIP - Temuco	-38.732639	-72.589222	114	1991/08/01	1991/08/31	77	6.8	-6.4	-37	14.2	No	14.3
199109	GNIP - Temuco	-38.732639	-72.589222	114	1991/09/01	1991/09/30	127	9.7	-7.7	-53	8.6	No	7.8
199111	GNIP - Temuco	-38.732639	-72.589222	114	1991/11/01	1991/11/30	51	13.1	-9.0	-64	8	No	6.3
199112	DGA Report	-39.236313	-73.159537	0	2014/09/08	2014/10/20	-	14	-5.1	-34.2	6.6	No	7.5
PP-2	DGA Report	-38.954570	-72.081393	297	2014/09/09	2014/10/03	56.63	14.4	-7.1	-50.8	5.6	No	5.2
PP-3	DGA Report	-39.390882	-71.680195	407	2014/09/25	2014/10/28	254.81	13.5	-7.6	-55.8	5.1	No	4.4
PP-4	DGA Report	-39.272345	-72.408570	257	2014/09/15	2014/10/28	283.13	13.4	-7.0	-42.4	13.2	No	12.9
PP-5	DGA Report	-38.686418	-73.367191	83	2014/09/09	2014/10/29	141.56	17	-5.9	-35.3	12.2	No	12.5
PP-6	DGA Report	-38.407726	-73.008774	50	2014/09/23	2014/10/11	45.3	15.05	-8.1	-51.8	13.3	No	12.2
PP-7	DGA Report	-38.690567	-72.398747	190	2014/09/10	2014/10/04	42.47	16	-7.0	-44.3	12.0	No	11.6
PP-8	DGA Report	-38.650107	-72.022820	468	2014/09/10	2014/10/04	67.95	10.1	-7.8	-48.9	13.4	No	12.5
PP-9	DGA Report	-38.668009	-71.832530	1102	2014/09/10	2014/10/04	84.94	14.3	-9.9	-65.0	14.5	No	12.1
PP-10	DGA Report	-38.769904	-72.708381	69	2014/08/06	2014/10/28	396.38	16	-5.9	-35.8	11.3	No	11.7
PP-11	DGA Report	-38.741094	-73.003769	10	2014/09/08	2014/10/29	84.94	17.5	-5.9	-38.8	8.6	No	9.0
PP-12	DGA Report	-38.436559	-72.592615	190	2014/09/23	2014/10/11	45.3	21.2	-6.6	-44.6	8.4	No	8.3
PP-13	DGA Report	-38.307640	-72.111689	500	2014/09/29	2014/10/11	33.98	15.7	-8.4	-55.4	12.2	No	10.9
PP-14	DGA Report	-38.811384	-71.658960	600	2014/09/09	2014/10/03	50.96	14.8	-9.2	-66.8	7.2	No	5.3
PP-15	DGA Report	-39.090053	-72.930272	57	2014/09/08	2014/10/20	-	16.5	-6.0	-35.7	12.4	No	12.8
PP-16	DGA Report	-39.012574	-73.085269	38	2014/09/08	2014/10/20	130.24	15.1	-6.8	-40.1	14.4	No	14.2
PP-17	DGA Report	-38.884306	-73.250854	3	2014/09/09	2014/10/29	101.93	18	-6.1	-36.2	12.4	No	12.6
PP-18	DGA Report	-38.958658	-72.611054	104	2014/09/08	2014/10/20	198.19	16.1	-7.2	-44.9	12.5	No	12.1
PP-19	DGA Report	-38.561678	-72.599680	324	2014/09/23	2014/10/11	56.63	13.1	-8.8	-56.5	13.6	No	12.1
Rain	Held et al. (2017)	-39.2199	-71.8153	420	-	-	-	-	-7.79	-55.8	6.5	No	5.6

Data from IAEA/WMO (2018). Global Network of Isotopes in Precipitation. The GNIP Database. Accessible at: https://nucleus.iaea.org/wiser, and Chilean Ministry of Public Works, Dirección General de Aguas. Published in Estudio Hidrogeológico, Región de la Araucanía (2016).

A.4 PHREEQC code (^{13}C in the CO_2-$CaCO_3$-H_2O system)

```
#Initial composition of solution.
#Parameters can be adjusted to match different reservoir fluids.
SOLUTION
temp 100
pH 5 charge
C    1.7
Ca   1 Calcite 0
[13C] -17.60 permil
END

#Define a fixed volume gas phase and a CaCO3 phase.
#Volume can be adjusted to modify degassing rate.
GAS_PHASE 1
-fixed_volume
-vol 0.1
CO2(g)  0
[13C]O2(g) 0
SOLID_SOLUTION 1
Calcite
-comp Calcite 0
-comp Ca[13C]O3(s) 0
END

#Generate graph
USER_GRAPH 1
-headings               TC 13C(aq) 13C(CO2(g)) pH
-axis_titles            "TDIC, mmoles" "PERMIL" "pH"
-initial_solutions      false
-connect_simulations    true
-plot_concentration_vs  x
-start
10 GRAPH_X TOT("C")*1e3
20 GRAPH_Y ISO("[13C]"), ISO("R(13C)_CO2(g)")
30 GRAPH_SY -LA("H3O+")
-end
-active                 true
END

#Copy and paste the following block several times to sequentally degas fluid.
#Repeat until final conditions are achieved.
USE solution 1
USE gas_phase 1
USE solid_solution 1
SAVE solution 1
END
```

Appendix B – Rayleigh fractionation model

As water vapor in the atmosphere condenses to form precipitation (either rain or snow), fractionation of the heavier isotope ^{18}O relative to ^{16}O occurs. At equilibrium, the magnitude of fractionation is determined by the equilibrium oxygen isotope fractionation factor α. If the condensate is continuously removed from the air-mass as it ascends (open system fractionation), the isotope ratio of the vapor and condensate follows a Rayleigh-type distillation law, given by the equations:

$$R_V = R_0 F^{\alpha-1} \tag{B.1}$$

$$R_C = \alpha R_V \tag{B.2}$$

where R_V and R_C are the $^{18}O/^{16}O$ ratio of the water vapor and condensate, respectively, R_0 is the initial $^{18}O/^{16}O$ ratio of vapor, and F is the remaining vapor fraction. When expressed in the δ-notation, the above equations are equivalent to:

$$\delta_V = (1000 + \delta_0)F^{(\alpha-1)} - 1000 \tag{B.3}$$

$$\delta_C = \alpha(1000 + \delta_V) - 1000 \tag{B.4}$$

The isotope fractionation factor α is a function of the temperature during condensation and the phases involved. $\alpha(T)$ has been determined experimentally by Horita and Wesolowski (1994) for liquid-vapor equilibrium and by Majoube (1970) for ice-vapor equilibrium. While some of the condensate may form as ice at temperatures below 0 °C, condensate in the atmosphere more commonly occurs as supercooled liquid by 20 °C or more below freezing point (Wallace and Hobbs, 2006). Thus, we apply the liquid-vapor fractionation factor for temperatures above 0 °C, the ice-vapor fractionation factor for temperatures below −20 °C, and a linear mix of the two for intermediate temperatures, such that there is not an abrupt step in α as the system cools (Rowley, 2007).

Once the system reaches saturation, the remaining vapor fraction F can be expressed as the saturation mixing ratio of water over the initial mixing ratio (r_s/r_0), if $r_s \leq r_0$, where r_0 is determined by the starting conditions, and r_s given by:

$$r_s = \frac{0.622 \mathrm{e}_s}{p - \mathrm{e}_s} \tag{B.5}$$

where p is the atmospheric pressure and e_s is the saturation vapor pressure of moist air, calculated via the equations postulated by Buck (1981):

$$[1.0007 + (3.46 \cdot 10^{-6} P)]0.61121 \exp\left(\frac{17.502T}{240.97 + T}\right) \tag{B.6}$$

for liquid-vapor equilibrium, and

$$[1.0003 + (4.18 \cdot 10^{-6} P)]0.61115 \exp\left(\frac{22.452T}{272.55 + T}\right) \tag{B.7}$$

for ice-vapor equilibrium, where T is the temperature in degrees celsius, and P is atmospheric pressure in kPa.

From the equations described above we can conclude that F and α depend entirely on the temperature and pressure of the system. For our model, we consider increments in altitude of 1 m and calculate the corresponding changes in P-T, assuming pseudoadiabatic cooling at each step (no loss or gain of heat except due to the condensation of water vapor). The decrease in pressure with altitude is approximated by:

$$p \approx p_0 \exp\left(-\frac{z}{z_0}\right) \tag{B.8}$$

where p_0 is the pressure at sea-level (101.235 kPa) and z_0 is scale height (8000 m). The change in temperature with height depends on whether or not condensation is occurring. As the initial air-mass water vapor ascends, before condensation begins, vapor cools at a constant rate (dry adiabatic lapse rate). At temperatures below dew point, the release of heat from condensation decreases the cooling rate of the air parcel, and cooling follows the moist adiabatic lapse rate. The rate of cooling is given by the well-established functions (American Meteorological Society, 2018):

$$\Gamma(m) = \begin{cases} \frac{g(1+r)}{c_{\mathrm{pd}}+rc_{pv}} & \text{if } r_0 \leq r_s, \\ \\ \frac{g(1+r)(1+\frac{L_v r}{RT})}{c_{\mathrm{pd}}+rc_{pv}+\frac{{L_v}^2 q_s(\varepsilon+r)}{RT^2}} & \text{if } r_0 > r_s, \end{cases} \tag{B.9}$$

where g is gravitational acceleration, r is the mixing ratio of water vapor ($r = r_0$ prior to saturation, and r_s after saturation), c_{pd} and c_{pv} are the specific heats at constant pressure of dry air and water vapor, L_v is the latent heat of vaporization, R is the dry air gas constant, ε is the ratio of the gas constants of dry air and water vapor (≈ 0.622), and T is temperature. As we did for the isotope fractionation factor, α, we use the latent heat of vaporization of water at $T < 0\,^{\circ}\mathrm{C}$, of ice at $T < -20\,^{\circ}\mathrm{C}$ and a linear mix of the two at intermediate temperatures, to account for the presence of supercooled droplets.

The above described model calculates the isotope composition of condensate forming at cloud-level. In order to convert these values to precipitation at ground surface, we calculate the isotopic composition of precipitate as a volume-weighted mean of condensate over a 1 km thick parcel of air, centered at 1000 m above ground, where the weights are based on the amount of condensate formed in each step (Δr_s) (Rowley et al., 2001; Rowley, 2007). This altitude interval was selected because low-level flow (below ~ 1.5 km) near the Andes transports most of the atmospheric water vapor (Garreaud, 2009).

For border conditions, we use the monthly-average, precipitation-weighted data from Temuco weather station presented below, and an initial isotope composition of vapor in order to generate precipitation compatible with annual-average precipitation-weighted Temuco GNIP data ($\delta^{18}\mathrm{O} = -7.3$, see Supplementary Material A.1), shown in Table B.1

Table B.1: Climatic parameters at Temuco GNIP station used as boundary conditions for the Rayleigh-fractionation model.

	Annual	Summer (Dec–Feb)	Winter (Jun–Aug)
Temperature	12	17	10
Rel. humidity	0.83	0.75	0.85